IN SITU IMAGE CORRELATION MEASUREMENT OF GRAIN-LEVEL DEFORMATION FIELDS IN TWINNING MAGNESIUM

by

M. Ayça Telemez

B.S., Metallurgical and Materials Engineering, İstanbul Technical University, 2008

Submitted to the Institute for Graduate Studies in
Science and Engineering in partial fulfillment of
the requirements for the degree of
Master of Science

Graduate Program in Mechanical Engineering
Boğaziçi University

2013

This study is dedicated to two most wonderful and self-sacrificing women, my beloved grandmother Suna Özemre and my mother Nilgün Telemez, and the most understanding man, my father Ercan Telemez in my life. They are the meaning of my life.

ACKNOWLEDGEMENTS

Throughout my life, my parents Nilgün Telemez and Ercan Telemez who dedicate their life to me without hesitating, my uncle Hakan Özemre who sticks closer than a brother for me, and my grandparents Suna Özemre and Nurettin Özemre who looked after me devotedly in my childhood and youth, care about my thoughts, my values and stand by me in all circumstances. They always support me and make a great effort with me for my success. I am evermore indebted them for their unconditional love, support and sensibility during my life. I love them more than anything.

I would like to express my sincere gratitude to my thesis advisor, Assist. Prof. C. Can Aydıner, for his guidance, encouragement, support and patience throughout my study.

I would also like to thank to the members of the committee, Prof. Günay Anlaş and Assist. Prof. A. Özgün Konca, for their comments and suggestions for the development of my study.

I am also very grateful to my friends, Kenan Çınar for spending his time to help me about my study, and Mustafa Şengör for his help, friendship and understanding. He becomes my close friend and confident in a short time, even though we are different.

And finally, I am very thankful to my friend, Cumali Özgür Karadeniz for his support, perceptiveness and being with me every time I needed during my university life. He always believes in me and stands by me with his endless patience. This becomes a big motivation for me whenever I lose it.

ABSTRACT

IN SITU IMAGE CORRELATION MEASUREMENT OF GRAIN-LEVEL DEFORMATION FIELDS IN TWINNING MAGNESIUM

In this study, *in situ* digital image correlation (DIC) has been utilized for full-field strain measurements in a hexagonal close-packed (HCP) AZ31 magnesium alloy at both macroscopic and microscopic (crystallite) length scales. Emphasis has been on examining the influence of twinning in the deformation behavior of polycrystalline magnesium. Although there is an abundance of *ex-situ* studies, few studies have employed *in-situ* DIC to investigate the micromechanics of the HCP twinning at the grain length scale. The loading mode has been uniaxial compression and the experiment was carried out on a textured sample to promote twinning activity. The experimental setup contained two optical systems (micro-scale and macro-scale) that acquired images from two orthogonal faces of the sample, providing volumetric deductions with this surface technique. The microscopic measurement surface has been prepared with metallography to reveal grain boundaries prior to the experiment to relate grain morphology with measured deformation patterns. The microscopic DIC revealed grain-scale shear bands whose collaborative activity appeared at the sample-scale as two macro-scale shear bands families that are oriented $\pm 45°$ to the loading axis. This shows that the strain heterogeneity is observed excessively at any length scale and a representative volume element cannot be defined for this material. The DIC analysis on the macroscopic imaging face has shown that macroscopic shear bands are not surface incidents, but volumetric formations. The orientation of these bands is associated with the texture of the material. At the micro-scale, the shear bands that extend over several grains follow grain boundaries rather than cutting through the grains, an observation commonly supported by literature. The DIC analysis is invalidated on twin bands when they sufficiently alter the DIC pattern with a surface step. On the bright side, this allows an automatic tracking of the twin formation. It is apparent that the zones of very high twin activity match with the zones of very high strain localization. Thus, twinning appears to play an important role in promoting strain localization.

ÖZET

İKİZLENEN MAGNEZYUMDAKİ DEFORMASYON ALANININ TANE ÖLÇEĞİNDE *YERINDE* DIGITAL IMGE KORALASYONU İLE ÖLÇÜMÜ

Hekzagonal sıkı paket (HCP) AZ31 magnezyum alaşımındaki tam alan gerinim ölçümü, *yerinde* dijital imge koralasyonu ile makroskopik ve mikroskopik ölçeklerde gerçekleştrilmiştir. İkizlenme olgusunun çok taneli magnezyumun deformasyon davranışı üzerindeki etkisi detaylı şekilde araştırılmıştır. Literatürde, *deney sonrası* çalışması fazlasıyla olmasına rağmen, tane skalasında HCP ikizlenmesinin mikromekaniğini *yerinde* DIC ile araştıran az sayıda çalışma bulunmaktadır. Tek eksenli basma deneyi, ikizlenme olgusunun sık görüldüğü tekstürlü bir numune üzerinde gerçekleştirilmiştir. Analiz sonuçlarından hacimsel çıkarımlar yapabilmek için, mikro ve makro optik sistemler kullanılarak numunenin birbirine dik iki yüzünden imgeler elde edilmiştir. Deformasyon haritası ile tane morfolojisi arasında bağlantı kurabilmek için, mikroskopik ölçüm yüzü, deneyden önce metalografik olarak hazırlanıp, yüzeyin tane sınırları ortaya çıkarılmıştır. Mikroskopik DIC analiziyle ortaya çıkan tane ölçeğindeki kayma bantları, mikroskopik imgeler birleştirildiğinde, yükleme yönüne $\pm 45°$ 'de konumlanan birbirine zıt iki makroskopik bant oluşturmuştur. Bu sonuç, gerinim heterojenliğinin her ölçekte yüksek derecede gözlemlendiğini böylece temsili hacim elemanının bu malzeme üzerinde tanımlanamayacağını göstermiştir. Makroskopik yüzdeki analiz, mikroskopik yüzde oluşan makroskopik kayma bandının sadece yüzeysel değil, hacimsel bir olgu olduğunu göstermiştir. Mikroskopik yüzeydeki kayma bandı, makroskopik yüzeyde yatay bir bant şeklinde ilerlemiştr. Bu bantların oryantasyonu, malzemenin tekstürü ile birebir ilişkilidir. Mikro ölçekte, birkaç tane boyunca ilerleyen kayma bantlarının, tane içinde ilerlemek yerine tane sınırlarını takip etmeyi tercih ettiği gözlemenmiştir. İkizlenme bantları yüzeyde stepler oluşturarak DIC desenini değiştirdiğinden, DIC analizlerini ikizlenmenin olduğu bölgelerde çalışmaz duruma getirmiştir. İyi tarafından bakıldığında, bu olay ikizlenme bölgelerinin otomatik takibini sağlamıştır. İkizlenme aktivitesinin yüksek olduğu bölgelerle gerinimin bölgeselleştiği yerler birebir uyumlu çıkmıştır. Bu, ikizlenme olgusunun gerinimin bölgeselleşmesinde önemli bir rol oynadığını göstermiştir.

TABLE OF CONTENTS

LIST OF FIGURES

LIST OF TABLES

LIST OF SYMBOLS

a, c	Lattice parameters of HCP unit cell
C	Correlation coefficient
I	Recorded intensity at camera detector
K_0	Center point of the image correlation patch
u	Displacement along x-axis
u_x , u_y	Partial derivative of u with respect to x , y
v	Displacement along y-axis
v_x , v_y	Partial derivative of v with respect to x , y
ε	Infinitesimal strain
ε_M	Macroscopic strain
σ	Stress
τ_{rss}	Resolved shear stress
χ	Coordinate map between undeformed and deformed images
ω	Infinitesimal rotation

LIST OF ACRONYMS/ABBREVIATIONS

2D	Two dimensional
AFM	Atomic force microscopy
BCC	Body-centered-cubic
BEI	Backscattered electron imaging
DIC	Digital image correlation
EBSD	Electron back-scattering diffraction
EDM	Electrical discharge machining
FCC	Face-centered-cubic
HCP	Hexagonal-close-packed
ND	Neutron diffractioin
RD, TD, ND	Rolling, transverse, normal directions in rolled plate
RVE	Representative volume element
SEI	Secondary electron imaging
SEM	Scanning electron microscopy
SXRD	Synchrotron x-ray diffraction
XRD	X-ray diffraction

1. INTRODUCTION

1.1. Motivation

A polycrystalline aggregate is a material that is composed of many connected crystallites (grains). The majority of metallic and ceramic materials used in engineering are polycrystalline aggregates, which are usually analyzed with the assumptions that they are isotropic and homogeneous. However, this *continuum* analysis is associated with the macroscopic scale and, when the material is viewed at the crystallite level, the picture becomes very complex. Since crystallites are elastically and plastically anisotropic, they constantly struggle among themselves trying to find common ground in satisfying equilibrium and compatibility. This means the microscopic (crystallite-level) stress and strain fields are, as a rule, heterogeneous. The simplistic picture in the macro-scale model comes from the fact that each continuum point is associated with a volume (representative volume element) that contains sufficient number of crystallites such that the microscopic stress variation can average out [1]. However, in terms of understanding the fundamental mechanisms of deformation and failure, micromechanical investigations of material behavior are crucial. Understanding of stress variation among and inside the grains (inter-grain and intra-grain stress fields) allows developing more fundamental models that extend our material design and prediction capability. Such models account for physics at the microscopic length-scale, e.g., they account for the activity of individual slip systems inside a grain [2,3]. Hence, plastic strain is a combination of dislocation activity in multiple slip systems.

Though plastic slip (coordinated dislocation activity) is the major deformation mechanism in crystalline matter, a mechanism called ‘deformation twinning’ gets also activated particularly in metals that don’t have cubic symmetry. For hexagonal-close-packed metals (HCPs: Titanium, Magnesium, Zirconium, etc.) with pronounced plastic anisotropy, emergence and growth of a twin contributes to deformation along the directions where slip activity is very hard**.** Twinning [4], a very interesting mechanism where a band of the crystallite becomes the mirror image of the rest, is distinctly different

from slip. It occurs suddenly and abruptly, comes with a very high transformation (eigen) strain and is directional, namely, if it operates for one sense of shear, it doesn't for the opposite sense. Consequently, in a polycrystalline aggregate in which certain grains exhibit twinning, the level of deformation heterogeneity and complexity is considerably higher. Macroscopically, twinning underlies unusual mechanical behavior like serrated stress-strain curves [5] and pronounced tension-compression anisotropy. Clearly, a fundamental understanding of deformation twinning and the intra-grain/inter-grain stress fields associated with it is necessary to better model these materials.

Experimentally though, the tools to *in situ* examine the micromechanics of HCP twinning are few. Diffraction methods such as neutron diffraction (ND) [6-10] and high energy synchrotron x-ray diffraction (SXRD) [11] provide volumetric measurements on this phenomenon. Neutrons can distinguish parent grains and their twin 'children' on highly textured samples, giving an average elastic stress data for both. ND does not directly investigate twinning at the grain level; it provides averages over grains of certain orientations in the entire sample volume. On the other hand, SXRD experiments [11] that uses the three-dimensional x-ray diffraction technique can get data from an individual grain and the actual twins that belong to this grain. However, working on a statistically significant number of grains is difficult in this otherwise very powerful technique. Further, results of this technique are averaged over the grain volume, meaning there is no sub-grain resolution.

Sub-grain resolution, on the other hand, is provided by recent surface microscopy studies with full field strain mapping. The strain field is evaluated by comparing the deformed image to the undeformed image through techniques like digital image correlation (DIC). Efstathiou *et al*. [12] have provided an extensive literature summary in this field, while investigating heterogeneous strain fields in HCP Titanium *ex situ*. The studies in this field have targeted deformation heterogeneities in cubic and HCP metals; examined the size of the representative volume element in actual material systems and was used to confirm micromechanical models [12-18]. These are typically *ex situ* studies but the work by Padilla *et al*. [19] is an *in situ* study on high-speed loading of an HCP Zirconium alloy. However, here, twinning is marginally observed and considered, and the emphasis is on

strain localization bands concentrated at the grain boundaries. The observation of strain localization at the grain boundaries is a recurring theme in this literature. The statistics provided in this study comprised several hundred grains but *ex situ* studies with varying magnification can provide much higher statistics (e.g., [12]). Twinning is also studied with *ex situ* micro DIC in another work by Efstathiou *et al.* [20] on Hadfield steel, on a single crystal sample.

An *in situ* micro-DIC study that particularly focuses on HCP twinning with sub-grain resolution is, hence, missing in literature. For this purpose, a Magnesium alloy, AZ31 for which twinning is a predominant (easily-activated) mechanism is considered. Targeting high spatial resolution as well as high statistics (microscopic data from the entire surface of a macroscopic sample), the study will target the elevated deformation heterogeneity that is caused by twinning.

1.2. Background

1.2.1. Basic plastic deformation mechanisms in HCPs

Dislocation motion constitutes the main mechanism of irreversible deformation in most materials. The dislocations do not glide on arbitrary planes or directions in the crystal, rather they, energetically, prefer gliding over certain planes and directions. Accordingly, densest atomic planes and close-packed directions are favored for slip activity. The slip plane and the slip direction in this plane are together called a slip system. The slip systems observed in a crystalline material depend on its crystal symmetry. In face-centered-cubic (FCC) and body-centered-cubic (BCC) crystals, there are 12 main slip systems that can be activated easily, i.e., at low stresses [21]. In the lower symmetry hexagonal-close-packed (HCP) material systems, however, the number of easily activated slip systems is only 4. This is less than the bare minimum (5 slip systems) that is required to generate an arbitrary plastic strain.

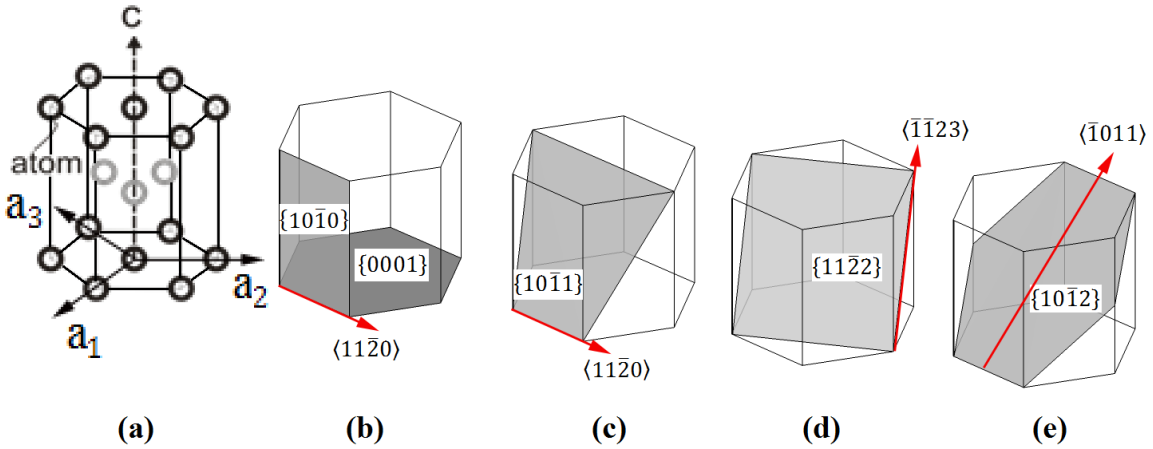

Figure 1.1. Basic atomic planes and deformation mechanisms in an HCP unit cell: (a) c and a represent four- axis or Miller-Bravais coordinate system. (b) Basal slip system $\{0001\}\langle 11\bar{2}0\rangle$ and Prismatic slip system $\{10\bar{1}0\}\langle 11\bar{2}0\rangle$ (c) Pyramidal slip system $\{10\bar{1}1\}\langle 11\bar{2}0\rangle$ (d) Pyramidal slip system $\{11\bar{2}2\}\langle\bar{1}\bar{1}23\rangle$ (e) Tensile twin system $\{10\bar{1}2\}\langle\bar{1}011\rangle$.

To convey further specifics of HCP deformation mechanisms, Figure 1.1a shows an HCP unit cell. Here,a_1, a_2 and a_3 are the unit cell axes that are separated by 120^o inside the basal plane (0001) and the *c* is the axis normal to (0001). The 4 easy slip systems are the basal $\{0001\}\langle 11\bar{2}0\rangle$ and the prismatic $\{10\bar{1}0\}\langle 11\bar{2}0\rangle$ slip systems shown in Figure 1.1b. The pyramidal $\{10\bar{1}1\}\langle 11\bar{2}0\rangle$ slip system (Figure 1.1c) is considerably harder to activate. However, regardless, in all the three slip systems mentioned; the slip direction is one of the *a* axes ($\langle 11\bar{2}0\rangle$ close-packed directions). Consequently, plastic slip in any one of these systems is incapable of producing deformation along the *c* axis. The only slip system that allows a deformation component along the *c* axis is the <c+a> pyramidal $\{11\bar{2}2\}\langle\bar{1}\bar{1}23\rangle$ slip system (Figure 1.1d), that can only be activated at high stresses.

Given the ensuing difficulty of deformation along the *c*-axis, another deformation mechanism called ‘deformation twinning’ is frequently observed in HCPs.

1.2.2. Deformation Twinning

Deformation twinning is the abrupt reorientation of a band in a stressed crystallite such that the atoms of the band form a mirror image of the original lattice with respect to a crystallographic plane called the 'twin plane'. The reoriented band is called the 'twin' and the crystallite of the original orientation is called the 'parent'. Figure 1.2a presents the twinning geometry for Magnesium, the HCP metal chosen in this thesis since it heavily employs the $\{10\bar{1}2\}\langle\bar{1}011\rangle$ tensile twin. Accordingly, the twinning shear occurs along $\langle\bar{1}011\rangle$ direction in the $\{10\bar{1}2\}$ plane at a characteristic strain value of 0.131 that reorients the c-axis of the twin zone almost perpendicular to the c-axis of the parent [22,23].

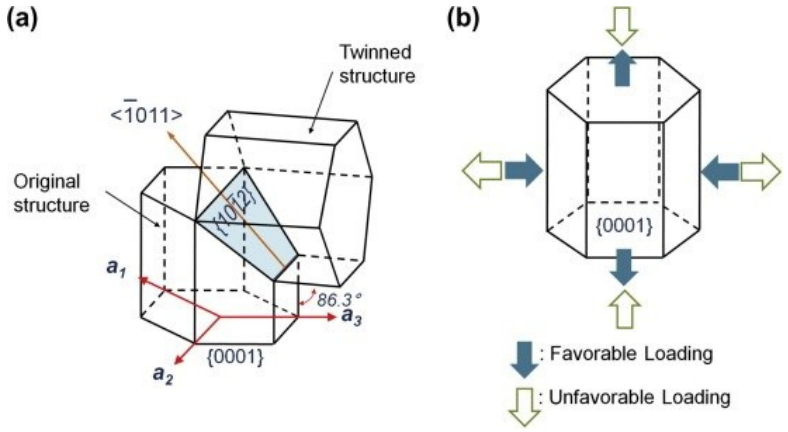

Figure 1.2. $\{10\bar{1}2\}\langle\bar{1}011\rangle$ tensile twinning in Magnesium (reproduced from [24]): (a) The twinned lattice is positioned with respect to original lattice at an angle of 86.3°, (b) uniaxial loading senses that favor twinning (bold arrows) and that preclude twinning.

For Mg with c/a ratio less than √3, the twin direction is specifically $\langle\bar{1}011\rangle$, not the opposite sense $\langle10\bar{1}\bar{1}\rangle$, since twinning is directional. In this particular case, the twin formation causes positive strain along the *c* axis, and hence, it is called a 'tensile twin'. Conversely, for an HCP metal with c/a > √3, twining about the $\{10\bar{1}2\}$ plane contracts the material along the *c* axis, and hence these metals undergo $\{10\bar{1}2\}\langle10\bar{1}\bar{1}\rangle$ compressive twinning. The directionality of twinning places a strict condition on the type of uniaxial loading that can activate this deformation mode. For Mg, as shown in Figure 1.2b, tensile loading along *c* axis or compressive loading normal to *c* axis can produce twins [4]. In a

polycrystalline compression sample, as we will utilize in this thesis, this means grains whose *c* axis are perpendicular to the compression direction will tend to exhibit twinning.

Nucleation of deformation twins can explain the idea that twins originate from a statistical distribution of defects in the grain boundaries and are activated by local stress at the grain boundaries [25].

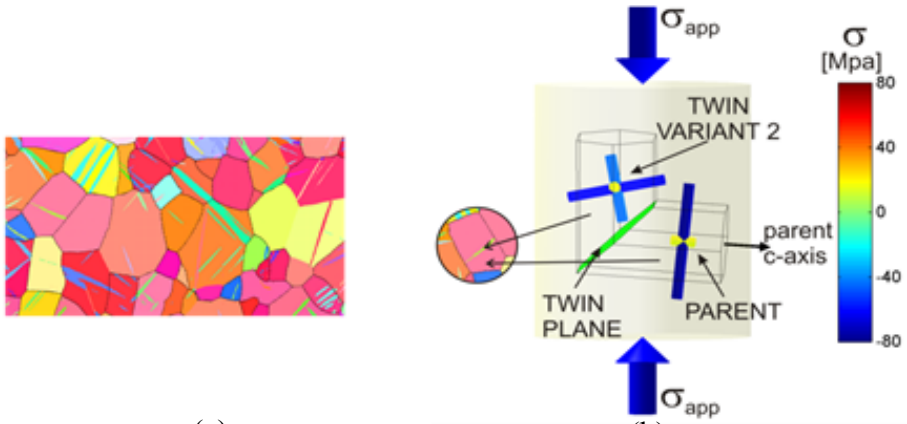

Figure 1.3. (a) A representative OIM (Orientation Imaging Microscopy) micrograph showing lamellar morphology of twin bands inside grains, (b) Under a compressive stress, orientation of the hexagonal unit cells of a twinning grain (parent) and the activated twin variant studied with synchrotron X-rays [11]. The length of the arms in the shown measured stress triads is proportional to the stress value.

Figure 1.3a shows twin bands inside a representative OIM micrograph reproduced from [11]. The bands morphologically lay parallel to the twin plane. Figure 1.3b details a synchrotron X-rays study of the same reference that details the stress interaction of the parent and the twin. Inside the parent, the $\{10\bar{1}2\}\langle\bar{1}011\rangle$ system has six variants that can be pictured by rotation the plane by 60º inside the hexagonal unit cell. The one with the highest resolved shear stress (τ_{rss}) will typically be activated. At times two twin systems have similar τ_{rss} and both can be activated. The figure shows that the stress value inside the activated twin variant (numbered 2) is drastically different from the parent. Particularly, the stress along the compressive axis is relaxed considerably.

1.2.3. The Digital Image Correlation Method

1.2.3.1. Principle. Digital image correlation (DIC) method is a full-field deformation measurement technique that works by comparing deformed and undeformed digital images of the sample surface [26-28]. The images can be obtained by a variety of techniques such as electron microscopy, optical microscopy, atomic force microscopy, etc. In each case, DIC relies on a characteristic pattern on the measurement surface that creates intensity variation in the image. If this pattern does not originate from the topographic features of the surface, it should be formed by the techniques detailed in Section 1.2.3.2. Owing to the intensity variation, the recorded intensity of each pixel in the image labels a corresponding point on the material surface. Consequently, the point's deformation can measured by locating it in the undeformed and deformed images. It is, however, still not possible to track a single pixel uniquely; since, in general, multiple pixels have the same intensity values (In an 8-bit camera, the intensity values will be integers 0 to 255.). To overcome this difficulty, DIC tracks a subset of pixels over which intensity variation is unique [26,27,29,30]. This pixel subset will be called a "patch" in this document. It is usually picked to be square in shape which corresponds to a square zone on the sample surface.

As an example, deformed and undeformed image that is recorded by optical microscopy in this thesis is provided in Figure 1.4. The patch that is centered about grid point K_0 in the undeformed figure is searched and found in the deformed image. The search algorithm that starts from the undeformed pixel coordinates in the deformed image (the patch shown with dashed boundaries) is detailed fully in Section 3.2. Considering many patches on a finely spaced grid as shown in Fig 1.5, allows the full-field measurement of the deformation map by DIC.

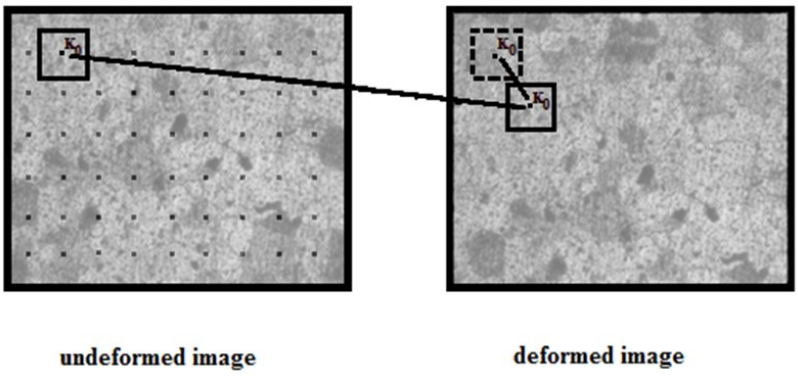

Figure 1.4. Undeformed and deformed region of image whereas K_0 is a certain point at the center of the patch.

The overall pattern's characteristics are crucial to obtain uniqueness and optimal accuracy with the method. The ideal DIC pattern that allows optimal tracking of patches should have an isotropic, non-repetitive, high contrast pattern [30]. A pattern of these characteristics is the "speckle pattern" shown in Figure 1.5 on the right. The first three images depict the pattern types that preclude ideal tracking in the DIC method. Further, in a patch to be tracked, the speckle size (a) should be a certain proportion of the patch size (L). The ideal value of a/L is around 0.2.

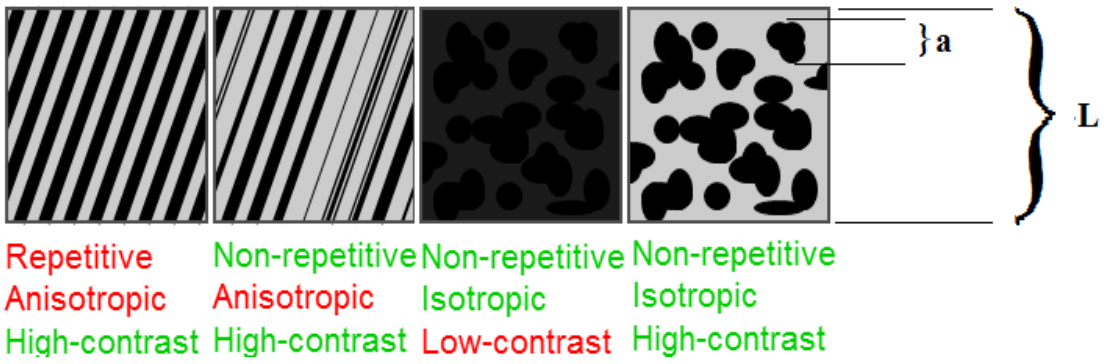

Figure 1.5. Three faulty patterns in comparison to the ideal pattern on the right end. L represents the patch size and α represent the speckle size.

1.2.3.2. Speckle pattern generation per observation technique. If an appropriate pattern does not already emanate from the original surface of the specimen, it has to be introduced with methods such as sputtering, physical deposition, particle application, air brushing,

deposition of fluorescent nanoparticles, imprinted gold web, and chemical deposition [12,31-34].

At the macro-scale, where the application of the DIC is widespread with optical cameras, patterns are typically introduced with spray painting [31,33,34]. In the micro-scale DIC applications, on the other hand, the method that can generate an ideal pattern is case-specific [12]. Further, the speckle size a will need to be physically much smaller to keep the a/L ratio admissible. Thus, a speckle pattern that is usable at the macro-scale will typically not work at the micro-scale. Usually though, existence of prominent microstructural surface features will make an applicable speckle pattern for all the measurement methods [31]. It should also be mentioned that the fundamental requirement from the pattern is that it has perfect adhesion to the surface. This way, as it deforms with the surface, there is no correlation loss [28].

The surface features that yield contrast in different types of microscopy varies. In addition, the required length-scale of the speckles depends on the magnification level. Thus, the techniques that are used to introduce effective patterns depend on the type of measurement (e.g., a pattern that works for electron microscopy might not work for optical measurements). There are three major types of microscopy utilized in DIC deformation measurement below the millimeter scale: (i) scanning electron microscopy (SEM), (ii) atomic force microscopy (AFM) and (iii) optical microscopy. In the following three paragraphs, the DIC applications of these three techniques are described in order, with references to the corresponding literature. The emphasis, here, is on the pattern generation for each technique.

Scanning electron microscope (SEM) is widely used at the 0.1-10 micrometer length scale (magnification range from x30 up to x10 000) [31]. For SEM use, the specimen must be stable under vacuum and electrically conductive. There are two basic imaging modes of SEM. One of them is the secondary electron imaging (SEI) and the other one is backscattered electron imaging (BEI). The SEI mode generates contrast in the images based on the surface topographic variation, while the BEI mode is less sensitive to surface topography. The image contrast in the BEI mode is due to sensitivity to different atomic

numbered elements. Both forms can be used to obtain images to identify the mode that will reveal better patterns for DIC analysis. The following SEM studies exemplify the use of *in situ* DIC for samples under mechanical load. Jin *et al*. [31] have considered two cases: The first one characterizes the mechanical properties of LIGA specimens at the micro-scale and BEI mode is used to obtain images. The second one is carried out to study the strain concentration around the crack tip of aluminum fracture specimens. Since both BEI and SEI modes do not provide sufficient contrast based on surface topography, the pattern is formed by sputtering gold particles on the surface. Scrivens *et al*. [32] have defined two methods to provide random patterns with thin film deposition onto metallic and polymeric materials within the range of 50-500 nanometers. In the first method, vapor deposition or ion implantation are used to apply thin films of metallic materials (Au, Ag, Cu, and Cr) to substrates. It provides high contrast random patterns with different morphologies. In the second, a simplified UV photolithographic method is used to apply thin films of metallic materials containing gold and silver to the materials. Sutton *et al*. [28], also considered two methods to form the speckle pattern depending on the SEM magnification. Lithographic pattern is applied for low magnification (1–20 μm pattern size) and rearranged nano-coating is applied for the high magnification (50–250 nm). Dautriat *et al*. [35] considered compression test on Estaillades limestone samples. They employed DIC at two length scales (using both SEM and optical microscopy) to identify the damage localization and reveal the characteristic structural heterogeneities. They utilized gold-coating to introduce the pattern for SEM observation. Collette *et al*. [36] also employed the same technique of pattern generation. Tanaka *et al*. [37] utilizes DIC with field emission scanning electron microscope. Here, pattern is generated by electron beam lithography.

When nano-scale deformation measurement is considered, atomic force microscope (AFM) is favored [31,38]. The AFM forms the image of the surface topography through a raster scan of the AFM probe. By definition there is no pattern to be introduced in AFM-DIC and one does not have to worry about an additional layer of material adhering to the actual material as in the other cases. However, position errors due to non-linearity, hysteresis and creep of the AFM scanner lead to distortion of the image. The image distortions in the AFM-DIC technique create a disadvantage in accurate determination of local deformation displacement field and strain field. Li *et al*. [38] have characterized the

drift and spatial distortion errors of AFM images. They considered a 500 nm thick gold thin film sample coated on a silicon wafer. They achieved a high quality random pattern with 60 nm particle size.

The magnification of the optical microscope is limited and up to x1000 (sub-millimeter range) [31]. The magnification is physically limited by the optical resolution limit, which is of the order of the wavelength of the light that is used for imaging (visible light 400-700 nm yielding around 1 μm resolution limit). The following references are for microscopic use of optical imagery with DIC: In the book by Sutton *et al*. [28], the first relevant case is the examination of the surface deformation of a ductile polymer material. To form a black and white pattern, white spray paint is applied lightly to the specimen surface. A halogen light with infrared filter is used for the specimen illumination. Another application example in [28] considers a crack closure load measurement using AA8009 aluminum alloy during fatigue crack growth. Here, the speckle pattern is formed by two methods: In the first, e-beam lithography is applied using Tantalum. Secondly, filtered toner powder is applied to the surface for the speckle pattern. A fiber optic illuminator is used. Schreier *et al*. [39] have also used spray paint and toner powder for a random black and white pattern and a fiber-optic ring light source to provide the illumination. Efstathiou and Sehitoglu [20] have measured the local strain field via DIC. They explained how the strain hardening behavior is affected by twins and twin–twin intersections at the Hadfield steel. This study is particularly relevant for its proximity to our application in this project. Speckle pattern have been applied to the polished specimens' surface via painting with an airbrush. Padilla *et al*. [19] investigated the effect of local texture on the heterogeneous plastic deformation in a cross-rolled Zr 702 zirconium sample. Prior to *in situ* DIC, electron back-scattered diffraction (EBSD) detector in SEM, is used in this study to outline the grain structure and to produce orientation maps. DIC patterns for both micro and meso-scale images are formed by using 1 micrometer silicon particles to the surface. Heripre *et al.* [13] investigated Titanium and Zirconium Aluminide alloys using a gold deposited micro-grid pattern. The heat generation during plastic deformation is investigated by Bodelot *et al*. [15] at the crystallite length-scale on an austenitic stainless steel sample. Here, infrared thermography has been coupled with DIC, DIC used to measure the strain fields. The speckle pattern is formed by spraying black and white paint. Abuzaid *et al.* [40]

measured plastic strain accumulation in nickel-based super alloy, HastelloyX using ex situ DIC with very high magnification. They measure orientation maps via (EBSD) and make deductions by comparing slip traces revealed by SEM imagery and DIC deformation fields. Carroll *et al.* [41] studied fatigue crack closure on titanium fracture samples, investigating the crack tip at the macro-scale (1.1X, 4.3X) and micro-scale (14X). No speckle pattern is applied to the titanium surface since its own topography is sufficient. Hamilton *et al.* [42] studied a ferromagnetic shape memory alloy, NiMnGa alloys, to investigate stress-induced martensitic transformations. For the DIC measurement, the pattern is formed by spraying paint. Carrol *et al.* [43] studied HastelloyX for detailing methodology of overlaying EBSD orientation maps with DIC deformation maps. Here, the speckle pattern was introduced by depositing 1 micrometer Si particles. Tong *et al*. [44], in their investigation of plastic deformation in Al-5%Mg, used mist of white-and-black paint spray to form a pattern. Li *et al*. [45] measure the whole-field velocity distribution in the deformation zone in cold rolling.

1.3. Scope

In this study, digital image correlation method (DIC) is adapted to make in situ deformation measurements of mechanically loaded polycrystalline samples at the grain length scale. The study targets the consequences of twin formation in HCP deformation patterns. Magnesium alloy AZ31 is selected since it exhibits twinning at low stresses (~50 MPa). To further assist the occurrence of twinning phenomenon, the samples are picked with an appropriate crystallographic texture. Hence, a compression sample is cut from a rolled AZ31 plate such that the compression axis lies along the rolling direction.

The optical microscopy is chosen in this study as the in situ observation technique. Thanks to its applicability in routine laboratory conditions, compression samples will be loaded with a fully-featured mechanical loading machine and images can be recorded from multiple angles. Conversely, SEM operates at high vacuum, and the loading apparatus is typically severely compromised.

Observation with visible light is constrained by an inherent resolution limit at around 1 micrometer. The study will push the resolution to this limit utilizing a lens/camera combination where one pixel corresponds to 0.2 μm. To obtain further resolution inside grains, one can also resort to enlarging them. For this purpose, the grains will also be enlarged by heat treatment.

The study will not utilize EBSD to obtain grain maps. Instead, the surface is metallographically prepared to reveal grain boundaries. This allows making the link between grain morphology and micro-scale deformation patterns. The technique to introduce appropriate DIC patterns that are applicable at this length-scale will be investigated.

To obtain volumetric information from the sample, images from two orthogonal surfaces of the sample will be recorded during the in-situ experiment. To obtain high statistics from microscopic imaging, the microscopic lens will be scanned over the entire surface of the sample with a precision positioning setup.

In summary, the study will technically aim to develop the experimental tools to make in situ intra-grain strain measurements with an optical DIC technique over a statistically-significant number of grains. Scientifically, the aim is to utilize this system to evaluate the deformation patterns of an HCP alloy that exhibits deformation twinning.

2. EXPERIMENTAL

2.1. Sample Preparation

The stock material for AZ31 Magnesium Alloy (3wt% Al, 1wt% Zn) has been acquired from Alfa Aesar, USA, in the form of two hot-rolled plates with dimensions 300x300x6.35 mm, 100x150x9.52 mm. The rolling process inflicts a crystallographic texture in the plates. This means the crystallites that form the plate will tend to be oriented in specific directions, rather than having a random distribution of orientations.

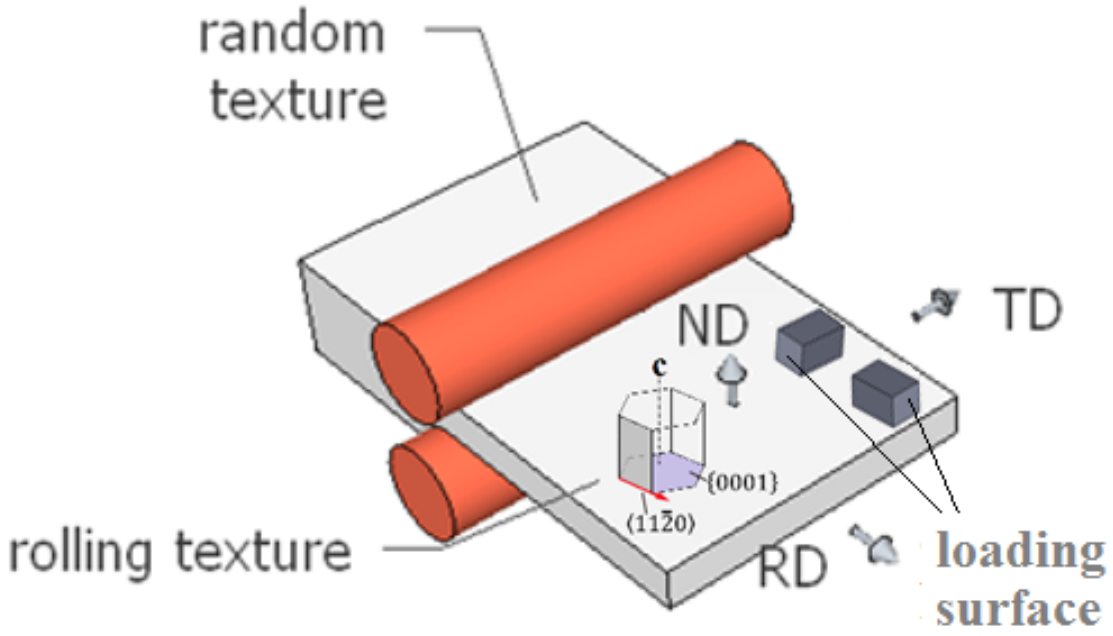

Figure 2.1. Direction definitions in the hot-rolled plate: RD (rolling direction), ND (normal direction) and TD (transverse direction). Random texture before the rolling process and the rolling texture (depicted with the unit cell) after the process are indicated in the sketch. Compression samples whose loading axes are aligned with the RD direction (right) and the TD direction (left) are also sketched.

A figure of the plate with the rolling direction (RD), transverse direction (TD), normal direction (ND) definitions are shown in Figure 2.1. The samples are cut from the

plate such that their loading axes are aligned with these 3 directions. For brevity, in this thesis an “RD-sample” will refer to a sample whose loading axis is aligned with the RD direction. Similar definitions apply to “TD-sample” and “ND-sample”. Figure 2.1 also sketches RD (right) and TD (left) compression samples.

The typical rolling texture in Magnesium is $\{0001\}\langle 11\bar{2}0\rangle$ texture [6,21,46]. Accordingly, grains with their basal planes perpendicular to ND and slip directions (*a* axis) parallel to RD are statistically favored. Since *c* axis is thus favored to be parallel to ND and given the load senses that favor twinning presented in Figure 1.2b, ND sample is expected to exhibit pronounced twinning in a tensile test and not in a compressive test. Conversely, twinning will be activated heavily in RD and TD compression samples.

Refinements on these nominal arguments will be presented in Section 4.1 which includes the X-ray diffraction determination of the actual texture of the employed samples.

2.1.1. Grain Enlargement

Most structural materials have smaller grain size (under 100 micrometer). Since this experiments are carried out at the grain level and patch size are typically limited to the range of 31-101 pixel squared which means 7,5- 25 micrometer (patch size must be several times smaller than the grain size), grain size around 100 micrometer is needed.

Firstly, the grain size of the Mg alloys is detected to decide whether heat treatment is necessary or not. In Figure 2.2, the microstructure photographs of Alfa Aesar AZ31 Mg Alloys are shown.

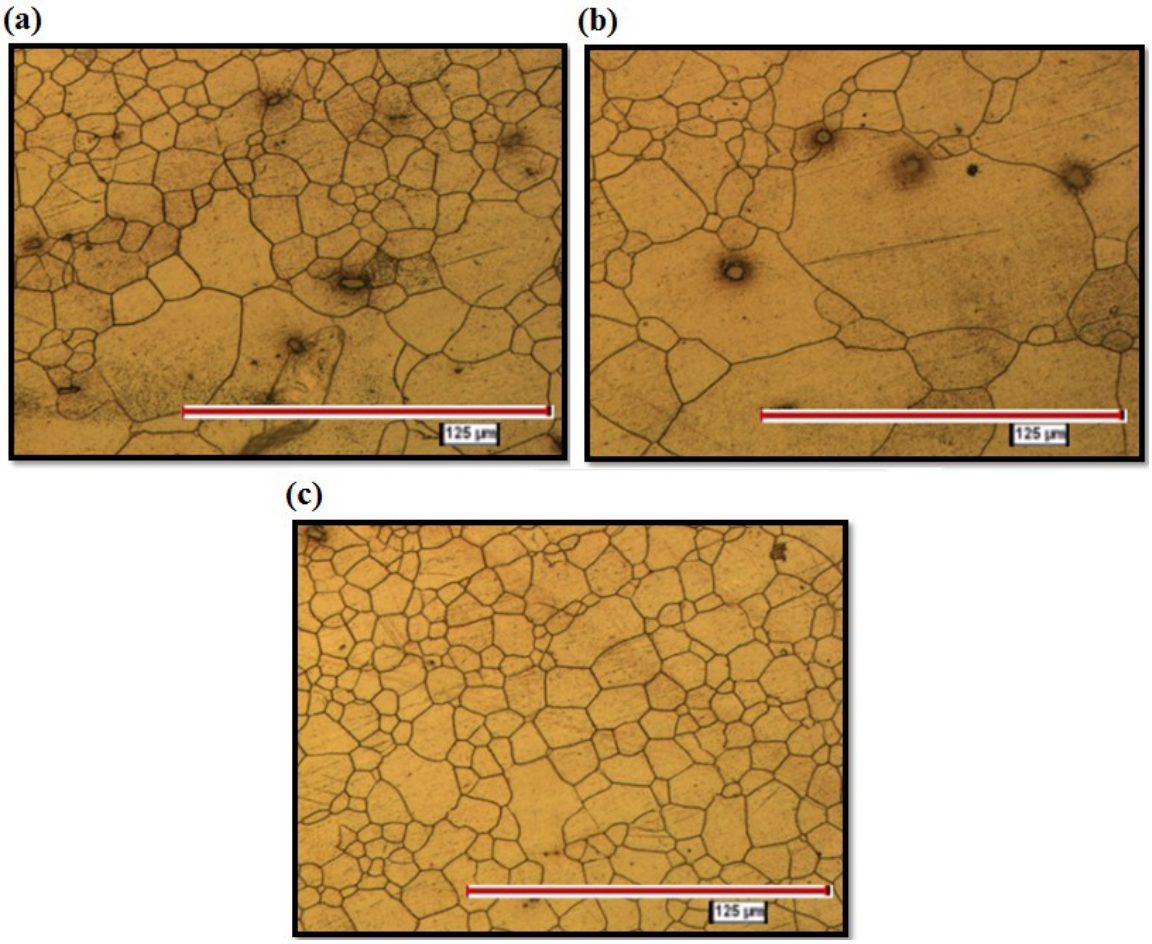

Figure 2.2. Microstructure photographs of AZ31.

As it is seen, the grain size changes on the average 20-60 micron also it exhibits non homogenous distribution. So heat treatment procedure is decided to apply for the grain growth. For this purpose, various combinations are tested. Mg alloy plates are annealed at 425^0 C for 6 hours, 500^0 C for 1 hour, 2 hours, 6 hours, 10 hours, 15 hours and 20 hours. The metallography is done to all these combination and they are compared to find which one gives the best and homogeneous growth. It is found that the best combination occurs at 500℃ and 20 hours. The microstructure photographs of annealed AZ31 Mg Alloys at 500℃ and 20 hours are shown in Figure 2.3. Since Mg is oxidizable, the argon gas is planned to be used for preventing oxidation. Despite mg is oxidized at 500℃, since oxide layer can be scraped easily with metallography (approved with experiments), the idea of using argon gas is given up.

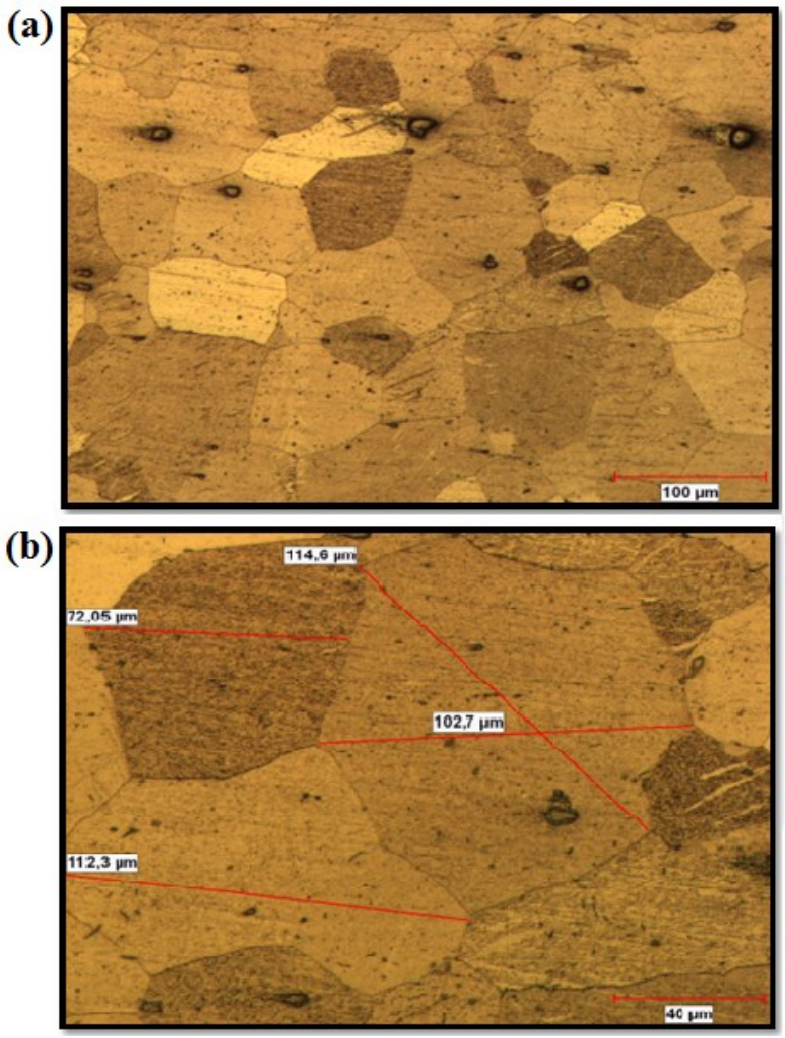

Figure 2.3. Microstructure photographs AZ31 Mg after the heat treatment.

2.1.2. Machining

After the grain enlargement operation, the samples are manufactured with wire electric discharge machining (EDM).

EDM is used to cut compression specimens of tetragonal prism shape and dog-bone tensile specimens from the plate (Figure 2.1). The compression sample's dimensions are 4 mm width, 6 mm length and 4 mm thickness. (Figure 2.4a) The tensile sample's dimensions are 12 mm width, 25 mm length, 2 mm thickness and 5 mm radius. (Figure 2.4b)

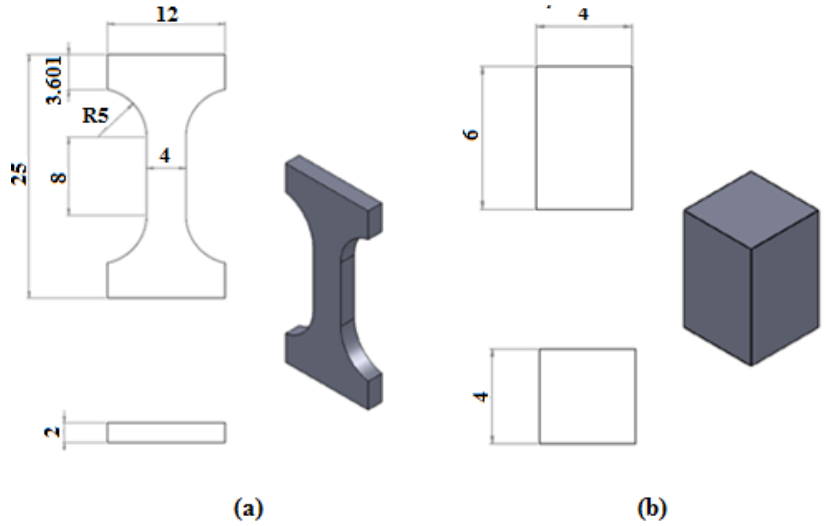

Figure 2.4. (a) Dog-bone shape tensile specimen. (b) Tetragonal prism shape compression specimen.

2.1.3. X-ray diffraction

X-ray diffraction (XRD) [47,48] is used to identify the crystal orientation distribution (texture) of the plate in Section 4.2. A two circle diffractometer is used that employs monochromatic X-rays of Cu-Kα wavelength. Figure 2.5 shows the θ-2θ configuration used to scan the sample for diffraction peaks. As such, while the sample is rotated by an angle θ the detector is simultaneously rotated by two times θ. This ensures that the diffraction signal will only come from crystallographic planes that are parallel to the sample surface.

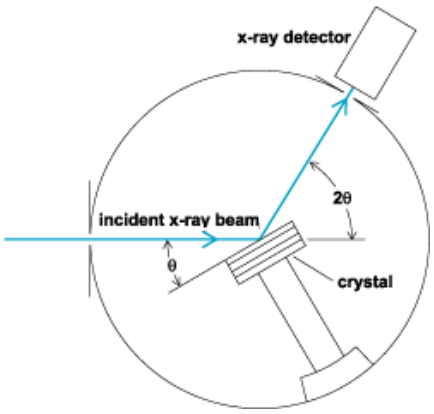

Figure 2.5. Basic X-ray diffractometer.

However, diffracted X-rays sensed by the detector, is only obtained at certain θ angles specific to each crystallographic plane. The interplanar spacing of the crystallographic planes and the scan angle θ should satisfy Bragg's law $n\lambda = 2d \sin\theta$ to yield constructive interference as shown in Figure 2.6.

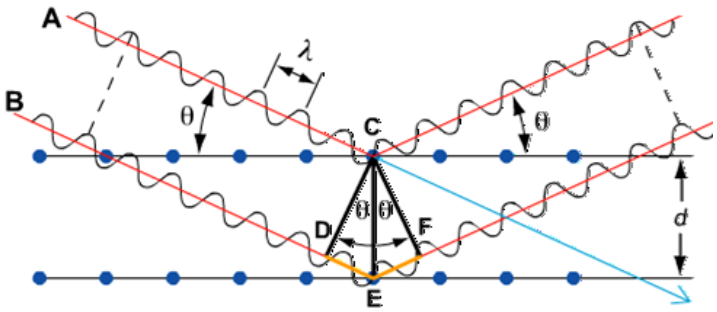

Figure 2.6. λ is wavelength of the monochromatic x-rays, *d* is the lattice interplanar spacing of the crystal, θ is the X-ray incident angle that provides constructive interference.

For a polycrystalline material, multiple grains will contribute to a certain diffraction peak since multiple grains can have the same crystallographic plane in diffraction condition.

2.1.4. Surface Preparation

2.1.4.1. Metallography. To obtain grain size, applying the metallography procedure correctly is necessary. Also by metallography, the characterization of Mg Alloys can be determined and after experiment hopefully, twinning can be seen. In metallography, there are some steps that must be followed. The steps of the procedure are given below:

- Cold Mounting: Many samples should be mounted for the ease of use to follow out other steps successfully during the sample preparation.
- Grinding: 240, 320, 600 grit sandpapers are sequentially applied to remove any EDM or oxide deposits or the extra material. The rate of the removed part depends on the number of particle contacts, the depth of cut and the shear velocity at the interface between the grinding medium and the work piece to prepare the sample for the polishing stage [21]. At every grit, the surface is sanded by occasionally altering the

surface's orientation with respect to the sanding direction. Only when the orientations of the scratches align, this stage is considered complete and the next grit is used.

- Polishing: The main purpose of the polishing step is to obtain a flat surface that is void of topographical features [21]. In each polishing steps, different micron scale solutions (finer and finer micron size at every turn) are used for removing a layer from the material that is damaged by the stage of surface preparation. In this project, sample is sequentially polished with 15, 9, 6, 3, 1, 0.3, 0.05 micron solutions. The procedure is carried on until all marks introduced in the grinding stage are cleared.
- Etching: Etching step is necessary to reveal the grain boundary, surface topography and the surface features by selectively removing the some part of the material surface [21]. For the AZ31 Magnesium alloy considered in this study, the etchant that yielded best results upon testing several other alternatives is acetic picral that contains acetic acid, picric acid, water, and ethanol.

In metallography, some difficulties are revealed. In the polishing step, the sample surface is covered with a chemical and is not polished. Finally, the best combination for polishing the surface is found. The velocity, force and chemical type exhibit very important role in polishing. For the best result, velocity must be around 150-200 rpm, force must be strong enough and ethanol must be used instead of water between the polishing step (15 to 0.05 micron). In addition to this, ethanol must be used with the polishing solutions.

Moreover, in the etching step, since the etchant that is used is very strong, the etching time is very short. In the eighth second, the etching is successful however in the ninth second it was mutilated and in the seventh second, the grain boundary was not visible yet. So the etchant should be applied to the AZ31 Mg alloy for an eight second.

After the etching step, the cutting process is applied for getting rid of the mounting part of the sample. The steps for the cutting process are:

- Coarse Cut: The lower back of the mounted sample's surface is cut in the diamond disk.

- Submerging the acetone: After the coarse cutting process, the sample with a thinner mounting part is submerged to acetone for easier fine cutting process. Acetone can change the property of the mounting part; it softens the epoxy so that it can be cut easier.
- Fine Cutting: After submerging the acetone, the thinner mounting part of the sample is ready for the fine cut. The fine cutting process is done with the sawing machine. The mounting part must be cut close to the sample as much as it is possible.
- Submerging the acetone again: After the fine cutting, sample with a very thin mounting part is submerged to acetone for removing the rest of the mounting part easily with hands.

After the cutting process, the sample is ready for forming a spackle pattern.

2.1.5. DIC Pattern Preparation

DIC Pattern can be formed with many different methods as it is mentioned in Section 1.2.3.2. In this thesis, this pattern is tried to form with two different methods, one of them is succeed. The unsuccessful method is paint with spray. The successful one is paint with airbrush. Whatever method is used, speckle size must be formed considering some criteria.

Size of the speckles in speckle pattern that is formed should be accordant with the sub-grain level. To obtain more accurate data for inter-grain and intra-grain, the patch size must be several times smaller than the grain size. The grain size of Mg plates reaches max 100 micron with heat treatment. By considering the relation between the speckle size and the patch size as it is mentioned in Section 1.2.3.2 (1/5 ratio with speckle size/patch size), it is concluded that the speckle size should be ~ 1 micron.

2.1.5.1. Paint with Spray. As a first attempt, the various spray paint is spraying to the sample surface directly and the speckle sizes of these paints are detected. For this purpose three kind of black paint are used.

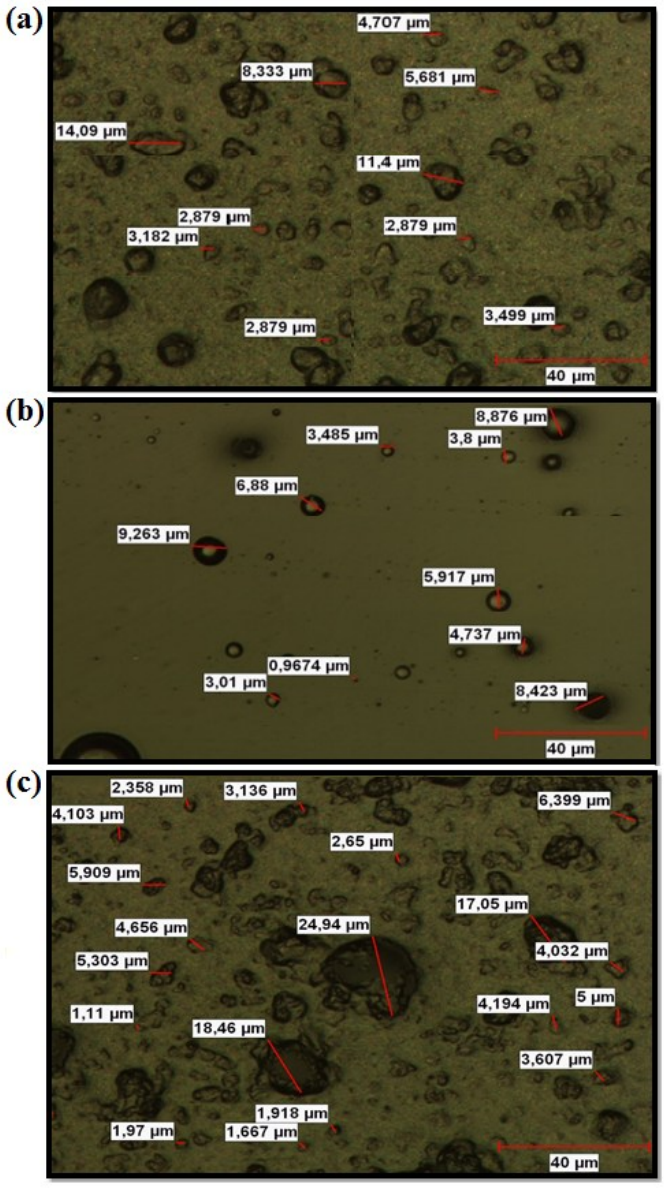

Figure 2.7. Three different kinds of black paint.

Many combinations (the distance and the spraying time is changed) are tried to find the best case for the pattern. However, the particle sizes of these paints can not be small enough (comparing 1 micron) and also not homogenous.

2.1.5.2. The paint with Airbrush. When the spraying method cannot form small speckles, a mechanism is needed to diminish the speckle size. After long researches, the Iwata Custom Micron B airbrush is purchased for this purpose (Figure 2.8) It has a very small nozzle and needle combination (.18-mm) so that it provides precise and accurate control of detail spraying.

Figure 2.8. Iwata airbrush used in the experiment.

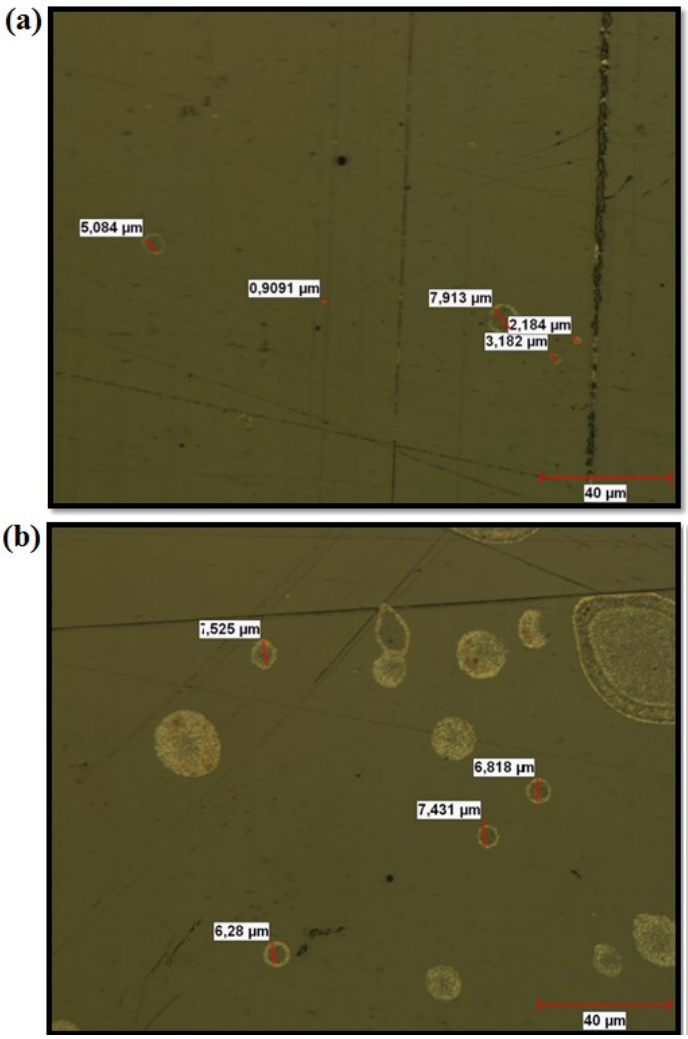

Figure 2.9. Paint droplet formed by airbrush.

When researching the proper paint and application scheme, Schmincke aero color airbrush professional paints are decided to be used Figure 2.9, acquired particles from Schmincke aero color paint by using Iwata airbrush can be seen.

However, when the airbrush is applied straightly, the speckles still cannot be small enough comparing spackle size that is wanted to obtain. So another mechanism is developed with airbrush. In Figure 2.10, shows the mechanism and describes how it works. Thus, different methods are searched.

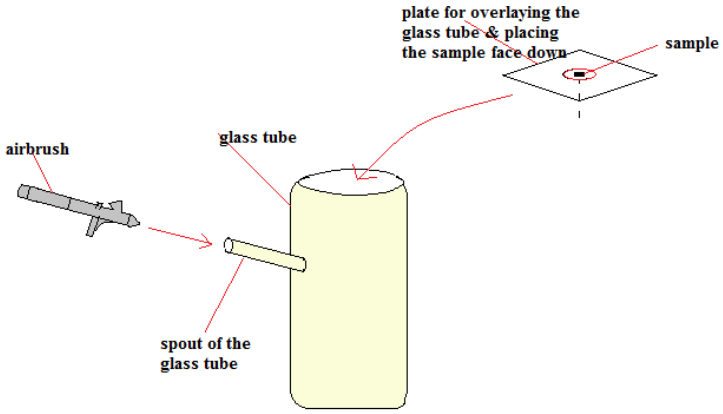

Figure 2.10. Equipment for forming the right spackle pattern.

The back surface of the sample is placed to the plate with an adhesive tape. Then, the plate is turned down and placed above the glass tube. The airbrush sprays the paint through the spout of the glass tube. With this operation, when heavy speckles are falling and adhering the glass tube, the light speckles (very small ones) are flitting in the air so that they reach the sample with the direction of reverse-gravity and adhere the sample surface. After this operation, 1 micron-size speckles are obtained.

2.2. Experimental Setup

2.2.1. General Setup

The general setup used in the experiment is shown is Figure 2.11. The Instron Micro Tester is used for the compression test. The optical cameras and the positioning stages is used for obtaining images from the sample surfaces.

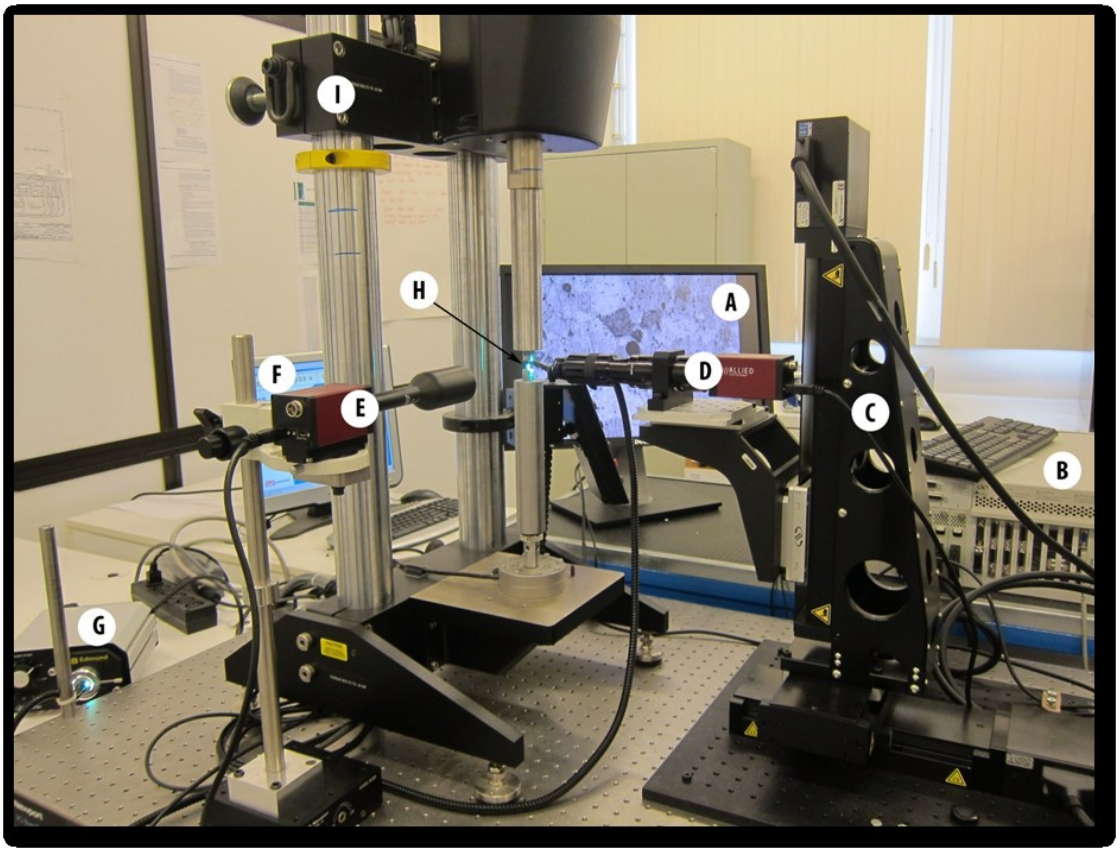

Figure 2.11. (A) Grains from an 1mm^2 area of the sample. (B) Controller of the x-y-z stages. (C) x-y-z stages. (D) The camera and the microscopic coaxial lens. (E) The camera and the macroscopic lens. (F) The computer system of the Instron Micro Tester (G) Light source for the coaxial lens. (H) The sample. (I) Micro Tester.

2.2.2. Positioning Stages

The micro-positioning equipment is set up. In the system, three dimensional positioning is provided by an x-y-z stage and above them there can be rotation stage (which will be inactive for this project of 2D DIC). In this project, the optical camera is placed above the bracket which is pinned to z stage. For this project, the most important feature of this system is that all three of the axes are connected to one controller and this controller can be controlled from computer. Since the camera is also controlled from the computer, all units of the system are interconnected. The desired positioning is a prerequisite for meso-scale studies (rather than macro-scale studies) for which the image is no displacement of the region with loading, a positioning system that is operated manually

could be enough. Since multiple regions (grain neighborhoods) of the sample are considered and each region is displaced with deformation, automated follow-up motion of the camera is needed for this in situ measurement. Further, to observe all areas of the sample, area scan (raster scan) is utilized with automated positioning. Many imaging routines are also adopted such as auto-focusing, image tracking, etc.

2.2.3. Optics

In this study, two optical lens/camera combinations are used simultaneously to obtain digital images in the *in situ* loading experiments. These combinations correspond to the two length scales targeted: the macro-scale and the meso-scale. In each, "AVT Pike F-505" 5 megapixel 2/3" CCD monochrome cameras are used where the macro-scale and meso-scale optics, labeled with (D) and (E), respectively, in Figure 2.11 are positioned to capture two neighboring faces of the sample. For macro-scale optics (E) whose close-up view is given in Figure 2.12, Edmund Optics 0.5X compact telecentric lens is used (field of view for this CCD is 17 mm). Hence, the entire sample face (4x6 mm) is captured in the frame.

Figure 2.12. Edmund Optics 0.5X compact telecentric lens + AVT Pike F-505 camera combination.

The meso-scale optics labeled (D) in Figure 2.11 targets the grain level, and appropriate microscopic lenses were procured from Navitar within the context of this thesis. The three components of these lenses (lens attachment, prime lens and adapter) that span a range of magnification levels and lighting options are detailed in Figure 2.13.

Figure 2.13. The three serial elements of the microscopic lens systems.

The magnification that can be obtained by alternate compositions of lens attachment + prime lens + adapter ranges between 0.7X-45X. The minimum field of view at highest magnification (45X) is 0.24 mm.

There are two prime lenses that can be used with the lens combination. In the first, the three member lens system (adapter + prime lens + lens attachment) has no coupling to the illumination, which is implemented with external members such as gooseneck illuminators. In the second system, the prime lens has an inlet for coaxial lighting, where light is fed to the lens system through a fiberoptic connection.

Figure 2.14. Navitar 2X lens attachment + 6,5 X coaxial prime lens + 2 X adapters + AVT Pike F-505 camera combination.

In the experiments of this thesis, an 18X magnification combination whose close-up is shown in Figure 2.14. The field of view in this magnification is 0.61 mm, or more precisely, 0.5x0.4 mm images fall on the 2/3” CCD.

3. NUMERICAL

3.1. Control Software

3.1.1. Area Scan, Autofocus

As mentioned before, automated follow-up motion system is needed since the multiple regions should be scanned. For this system, an area scan code is written. With this code the camera can scan the whole area step by step for the desired coordinates. At all stages, the images are captured from the area at this coordinate. Since the sample surface is at a slight angle to the camera, when the camera walks over it, working distance changes slightly. For this reason, multiple images are captured at the same coordinate and with an autofocus code the best image of this coordinate is determined. Then the camera is moved to the next coordinate and the same procedure is applied.

3.2. DIC Algorithm and Software

This section provides the mathematical and algorithmic description of the DIC method whose principle was sketched in Section 1.2.3.1. Consider point K, the point at pixel coordinate (x, y) in undeformed image. Upon deformation, this material point will displace physically. It will appear at a different point pixel coordinate K^* in the deformed image whose pixel coordinate (x^*, y^*). The corresponding displacements, (u, v) among point K^* and point K are defined in Equations. 3.1 and 3.2. χ is the position mapping from the undeformed image to the deformed image (Equation 3.3). Further, the intensity value of point K in the undeformed image and point K^* in the undeformed image are defined as $I(x, y)$ and $I^*(x^*, y^*)$, respectively. The working principle of DIC method is that $I(x, y)$ and $I^*(x^*, y^*)$ should match (Equation 3.4) [26,27,49,50].

$$x^*(x, y) = x + u(x, y) \tag{3.1}$$

$$y^*(x, y) = y + v(x, y) \tag{3.2}$$

$$K \rightarrow K^* = \chi(K) \tag{3.3}$$

such that

$$I(x,y) = I^*(x^*,y^*) \tag{3.4}$$

However, since it is not possible to track a single point, a subset of connected pixels (a "patch") is considered. The patch will typically be square in shape as introduced earlier in Figure 1.4. Accordingly, K_0 is defined as the center point coordinate $(\mathrm{x}_0, \mathrm{y}_0)$ of the patch in the undeformed image. After the sample deformation, K_0^* will be the new center point of the deformed patch at coordinate (x_0^*, y_0^*).

The deformed coordinate of an arbitrary point (x^*, y^*) in the patch can be expressed in terms of the center point coordinate $(\mathrm{x}_0, \mathrm{y}_0)$ and displacements with a Taylor Expansion

$$x^* = x + u(x_0,y_0) + \frac{\partial u(x_0,y_0)}{\partial x}(x - x_0) + \frac{\partial u(x_0,y_0)}{\partial y}(y - y_0) \tag{3.5}$$

$$y^* = y + v(x_0,y_0) + \frac{\partial v(x_0,y_0)}{\partial x}(x - x_0) + \frac{\partial v(x_0,y_0)}{\partial y}(y - y_0) \tag{3.6}$$

where the terms higher than the first derivatives are ignored (taking χ to be a linear mapping, higher order mappings are possible but rare [28]). The coefficients in the above expression, the patch center displacements and displacement derivatives are spelled out as

$$u = u(x_0,y_0), \qquad v = v(x_0,y_0),$$

$$u_x = \frac{\partial u(x_0,y_0)}{\partial x}, \qquad u_y = \frac{\partial u(x_0,y_0)}{\partial y},$$

$$v_x = \frac{\partial v(x_0,y_0)}{\partial x}, \qquad v_y = \frac{\partial v(x_0,y_0)}{\partial y} \quad . \tag{3.7}$$

From Equation 3.4, the intensity values of the deformed and undeformed patches should match; however, they will not be equal due to (i) minute changes in physical

conditions while recording the two images, (ii) the patch will be displaced and deformed by a fraction of a pixel, so the discrete data of the undeformed image cannot be exactly equivalent. That's why, the correlation coefficient C is defined in Equation 3.8 as the square-sum of the intensity errors for each pixel i in the undeformed patch where N is the number of pixels in the patch. The patch center displacements and displacement derivatives (parameters of Equation 3.7) are then optimized by minimizing C (for alternative measures of correlation coefficient, see [28]). Subpixel resolution is desired in displacement results u and v. Further, the deformed pixel coordinate for each patch pixel (x^*, y^*) in the term $I(x^*, y^*)$, will not be integers. The intensity of the deformed image, however, is recorded for each detector pixel. So, a single value corresponds to a finite region of material and the data is discrete in nature (Figure 3.1a). Consequently, interpolation (Figure 3.1b) is needed between data points of the patch in the deformed image to reconstitute a continuous pattern $I(x^*, y^*)$.

$$C = \sum_i^N [I(x, y) - I(x^*, y^*)]^2 \tag{3.8}$$

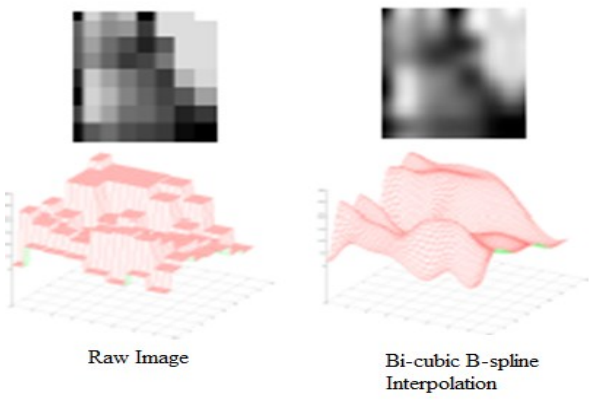

Figure 3.1. (a) Discrete data example (b) The data that undergos the bicubic Interpolation.

The DIC software used in this study is coded in Fortran and Python. While the algorithmic part of the software is written in Fortran and provides a fast binary for the rudimentary operation, preprocessing (input file preparation and submission) and post

processing (collecting results, evaluating derivatives, etc.) for multiple correlations uses a framework written in the Python scripting language.

The algorithmic part of the code has two main operation steps for tracking a patch (i) coarse optimization and (ii) sub-pixel (Newton-Raphson) optimization. The main input parameters admitted by the Fortran DIC engine for the correlation of each patch are defined and briefly explained in Table 3.1.

Table 3.1. The main input parameter in DIC Software.

Input Parameter	**Function**
nsub, msub :	**The patch dimension around K_0**
nrtx, nrty :	**Dimension of a search grid zone where the coarse optimization is performed**
ntrincx, ntrincy :	**Step size (the distance between two grid point) of the search grid zone**
nconfx, nconfy :	**Divider of the step size**
ishiftx, ishifty :	**The shift that is given to help the coarse optimization to find the K_0 in the right place.**

When comparing two images with the DIC method, firstly grid points (black dashed) are determined. These grid points are the center points of the patches where the six parameters of Equation 3.7 are calculated (Figure 3.2). The distance between the grid points should be judged in accordance with the spatial resolution desired in the full-field results.

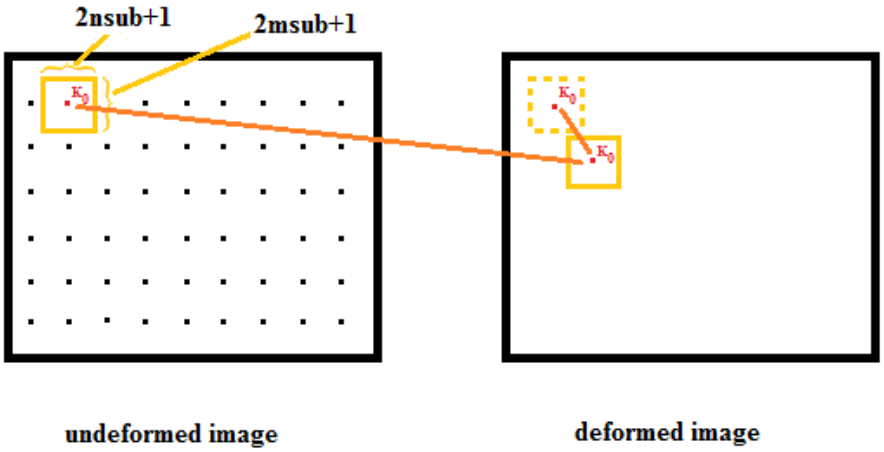

Figure 3.2. The grid point which are the center point of the patch whose size is $(2 \cdot nsub + 1) \times (2 \cdot msub + 1)$ in undeformed image and the deformation and the displacement of the patch in undeformed image after deformation.

To detail the coarse search process, K_0, one of the grid points in the undeformed image, will be considered. The patch size around this point is $(2 \cdot nsub + 1) \times (2 \cdot msub + 1)$ as shown in Figure 3.2. With the coarse search, the two parameters $u$and v are determined within 1 pixel, where the displacement derivatives are kept zero.

Figure 3.3 details the steps of the coarse search on the deformed image. Starting from the pixel coordinates of the patch in the undeformed image (K_0), first, the patch center is shifted by *ishift*, to bring the search center to the vicinity of the tracked patch in the deformed image. Let this new point be A.

A coarse search grid (not to be confused with the initial analysis grid) is formed around point A with a (2nrtx+1)(2nrty+1) dimension. The distance between each grid point is defined by parameters nrtincx, nrtincy. Then, centered about each coarse search grid point, (2nsub+1)(2msub+1) zones are considered. The correlation coefficient (Equation 3.8) is calculated for each zone and the best correlation is picked. The grid center point of best correlation is depicted as point B in Figure 3.2. Then a new coarse search grid is defined about B and the procedure is repeated. The new search grid about B is formed that the new nrtx, nrty is old nrtincx, nrtincy and the new nrtincx,nrtincy is reduced by nconfx

and nconfy. This procedure goes on until the nrtincx and nrtincy are equal to 1 (pixel resolution).

Let nconfx, nconfy be 2 and nrtincx, nrtincy be 4 in the first stage of coarse search (about point A) which typical entails a large grid with nrtx and nrty around 20. The best correlation of this stage is supposed to have a resolution of nrtincx by nrtincy. Hence, point A is supposed to be located within 4 pixels of the actual position. Consequently, the second stage (about the point B) search grid is reduced such that the new nrtx, nrty are 4 and the search is refined by nconfx, nconfy such that the grid spacings nrtincx, nrtincy are 2. In the third stage (after locating point C within 2 pixels), nrtx and nrty are set to 2 and the new nrtincx, nrtincy are reduced to 1. Consequently, at the end of this stage, the point is determined within one pixel resulting in point D.

Coarse search serves to find a good starting point for the displacement parameters *u, v*. Then fine optimization utilizing the Newton-Raphson algorithm ensues to determine the patch center displacement with sub-pixel resolution and allowing a better fit by optimizing all six parameters. Then all possible values of u and v within a range are tried with other 4 variables remains zero. The best comparison of u and v values will be u_1 and v_1. This approximation is based on minimizing C (correlation coefficient) that is mentioned in Section 1.2.3.1. The same procedure is repeated for u_x and v_y, within a range with u and v are set u_1 and v_1 and other two variables remains zero. The best comparison will set as u_{x1} and v_{y1}. Finally, after the process is done for the u_y and v_x when the other variables set constant and the best comparison is found and fixed as u_{y1} and v_{x1}, the first estimates of six parameters will be found. After that the procedure goes on for the u_1 and v_1 within a smaller range around u_1 and v_1 when others are fixed constant. This procedure continues until the C reaches its minimum value. Thereby, at the end of these optimizations the six parameters are obtained.

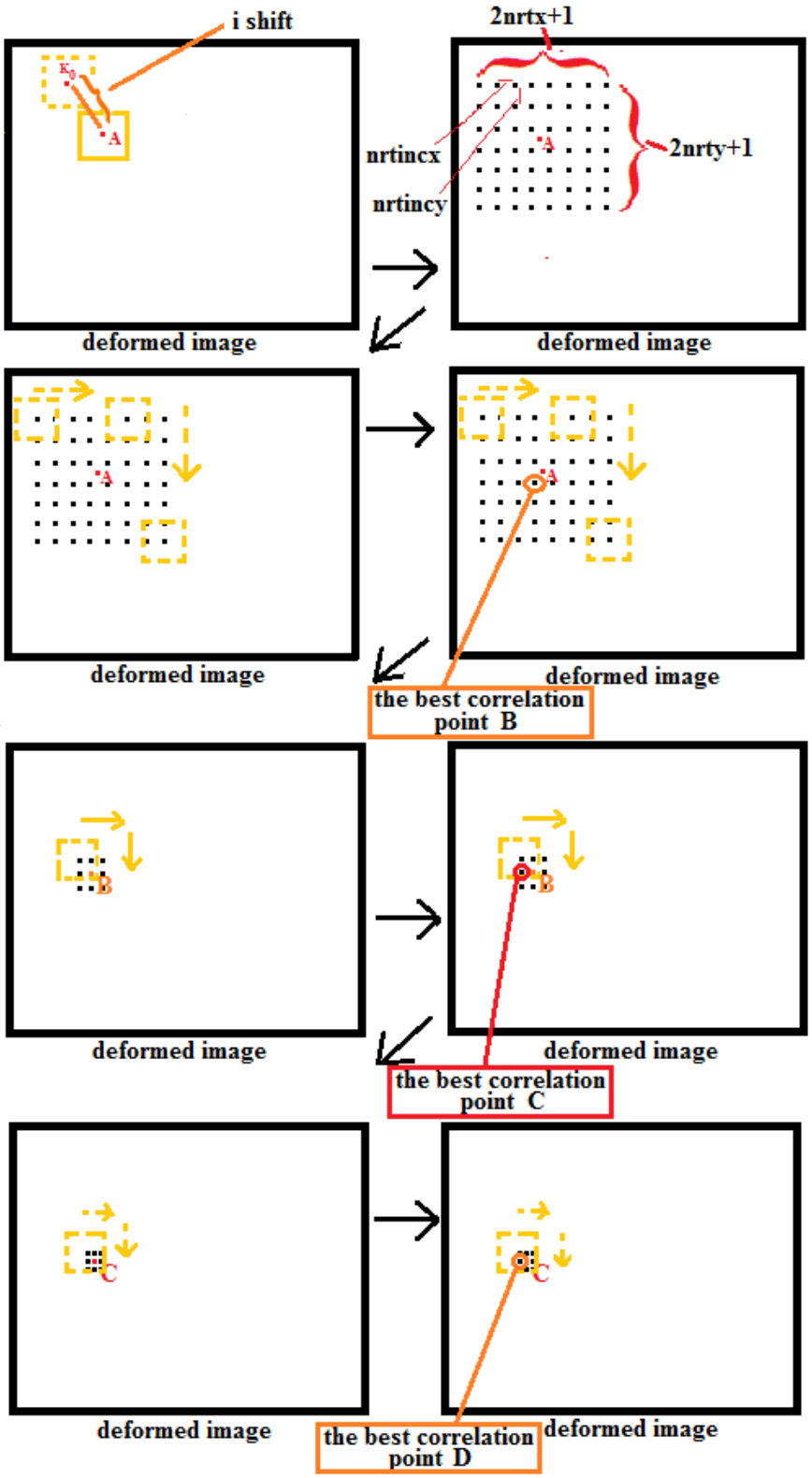

Figure 3.3. The coarse search steps expressions on the deformed image.

4. RESULTS & DISCUSSION

4.1. Determination of the optical setup

The AZ31 Magnesium alloy samples that are used for experiments (and, in general, metals) have a highly reflective surface following the metallographic surface preparation. In addition, illuminating the surface with a high intensity light source is a necessity to allow taking images from microscopic zones with reasonable shutter speeds. This might mean formation of shiny streaks on the sample surface due to specular reflection, which is severely detrimental for image correlation measurements.

To detail further, specular and diffuse reflection are the two constituents of light reflection from a surface. Reflection of light with the exact same angle as incident light is called specular reflection. Incident light will also cause a diffuse reflection where light is produced with equal intensity at all angles. The extent of specular reflection in comparison to diffuse reflection depends on the material and geometrical factors. Specular reflection requires a flat surface, but no matter how flat, certain materials (e.g., marble) will produce predominantly diffuse reflection. Polished metals, in contrast, will produce a high fraction of specular reflection. If, on the metal surface, specular reflection preferentially occurs at certain spots, anomalously bright zones will show in the images.

In this regard, two different lens systems are tested (Section 2.2.3) for image quality which correspond to the two possible illumination modes. The details of two systems are mentioned in Section 2.2.3.

In the first case with external illumination, the attempt was to avoid bright streaks by inhibiting specular reflection all together. Since, the fraction of specular reflection gets higher with incident angle (the best angle to favor specular reflection is 90º, i.e., normal illumination of the surface), incident light is applied at shallow angles. Even then, the specular reflection could not be avoided utterly. Figure 4.1, shows the best pictures that can be obtained with this lens which still suffer from anomalously bright spots.

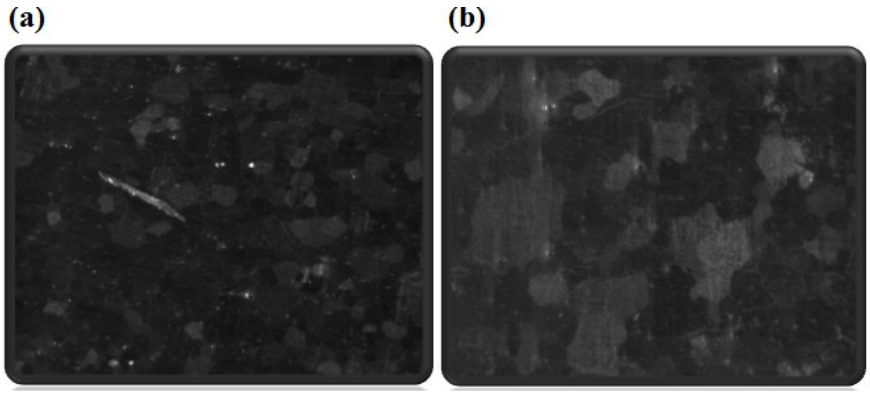

Figure 4.1. Images taken by normal lenses. (a) and (b) images are the best images taken with this lens.

The second lens system utilizes coaxial lighting, which is also the predominant lighting mode in all commercial microscopes. In a coaxial lens, the illuminating light travels along the axis of the lens and, hence, the incident rays are normal to the sample surface. Consequently, in effect, this mode corresponds to the specular reflection of the entire field: It utilizes specular reflection rather than attempting to avoid it which was the strategy in the external lighting mode. The images are high quality and have balanced lighting in this mode as shown in Figure 4.2 and coaxial lighting for the microscopic lens is also decided to be the preferred optics in this project. This mode also allowed the use illumination optimally and allowed reduced shutter speeds, which is crucial for sharper images.

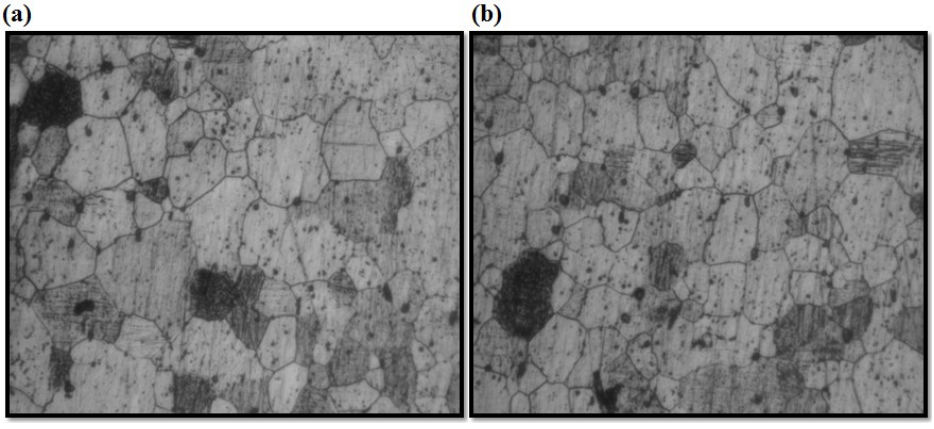

Figure 4.2. Images taken by coaxial lenses.

An important result of working in the reflective mode is that the intensity observed at the detector has little to do with feature color but rather feature morphology. Hence, the white pixels in the images likely correspond to zones of high surface flatness rather than, zones of material that is white in color. Such a white zone reflects visible light of all wavelengths by its definition but if it has appreciable surface roughness, it will appear black in the detector. When white speckles are sprayed to polished metal surface in an attempt to create white zones in the image, this has been the precise observation: The speckles appeared black since they cannot compete with the metal surface in terms of specular reflection.

4.2. Texture evaluation with X-ray diffraction

In Section 2.1.3, XRD method is mentioned in detailed. The XRD results for ND, RD, TD pattern is shown in Figure 4.3. It indicates the distribution of crystallographic orientation of grains in RD, TD, and ND sample with using 2θ values.

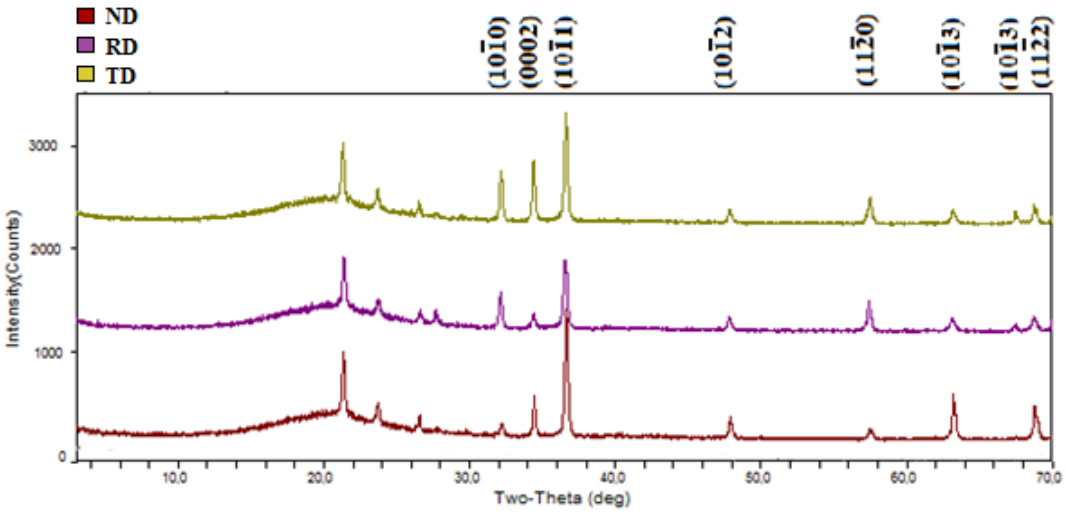

Figure 4.3. X-Ray diffraction patterns that are taken from three sample surfaces perpendicular to the RD (rolling direction), ND (normal direction) and TD (transverse direction). Miller indices of crystal planes that belong to AZ31 diffraction lines are indexed only.

The (0001) diffraction peak is forbidden; hence the first signal from the basal planes is the (0002) peak that is formed in the Figure 4.3.

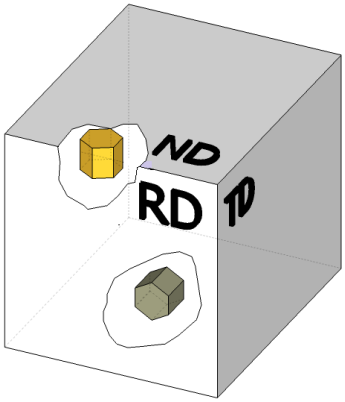

Figure 4.4. The sketch for explaining the peak meanings.

To sketch the use of diffraction for identifying texture, the contribution of two grains to the (0002) peak is considered. The grain whose basal plane is perpendicular to ND will contribute to the (0002) peak in ND diffraction pattern and the grain whose basal plane is perpendicular to the RD will contribute to the (0002) peak in RD diffraction pattern (Figure 4.4). While the strength of the (0002) peak in ND pattern shows that there are too many grains whose c axis parallel to the ND, the weakness of the (0002) signal in RD pattern shows the rareness of the grain whose basal plane perpendicular to the RD.

The typical rolling texture in Magnesium is $\{0001\}\langle 11\bar{2}0\rangle$ texture which means that the grains whose basal plane perpendicular to ND and slip directions (*a* axis) parallel to RD are predominantly exist in the sample.

The XRD results obtained from Figure 4.3 shows that grains whose *c* axis aligned with ND (basal plane perpendicular to ND) are predominant in the plate that is used in the experiment. However, the slip direction is not favored in the RD direction; rather it is aligned with the RD and TD evenly. This situation shows that twining mechanism is dominant in both RD and TD sample.

Since RD and TD samples behaviors are similar, ND sample behavior is different from the others in macroscopic scale because of different direction pattern (RD, TD, ND pattern). RD sample (Figure 4.5b) that has active twin mechanism exhibits ductile behavior more than ND sample (Figure 4.5a) that forms twins difficultly.

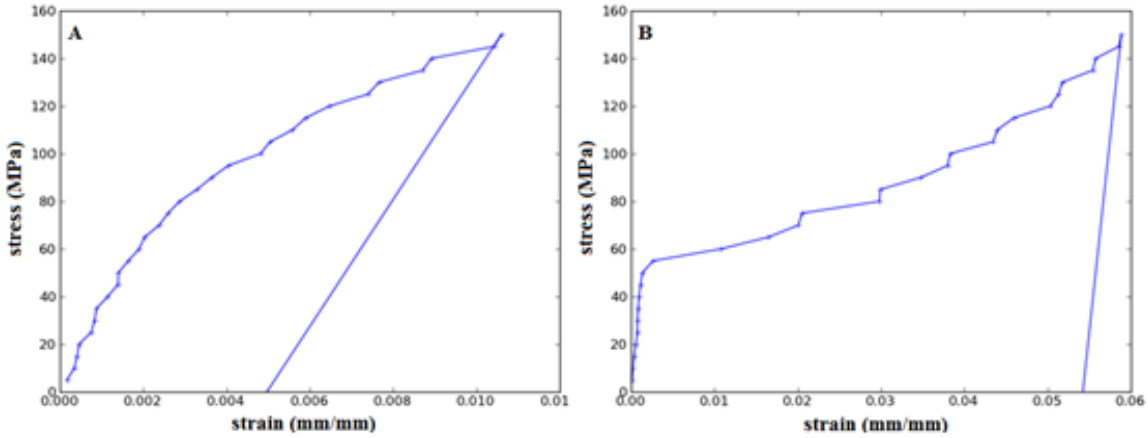

Figure 4.5. Stress-strain diagram of samples whose loading axes are (A) ND (Normal Direction), (B) RD (Rolling Direction) with macroscopic DIC.

4.3. Microscopic-Macroscopic in-situ DIC compression experiment on an RD sample

4.3.1. Detailed Procedure

These procedures include both microscopic and macroscopic experiment steps.

The following are the steps prior to the introduction of the speckle pattern:

(i) Clean the optical element including detector face, lens face etc.
(ii) Measure the sample dimensions with a caliper and record them.
(iii) Adjust the steel ring that connects the bottom compression rod with the load cell connector such that the ring bears the load. (This ensures the vertical alignment of the compression rod.)
(iv) Fix the cameras to their corresponding stages and tighten their connections. Through their video recording, check if they are easily affected from minor contact.

(v) Strain relieve the Firewire cables of the cameras. Ensure enough slack on the stage camera against the motion of the X-Y-Z stages.

(vi) Run the AVT Smartview software for the macro imaging camera (in the other (second) computer) and choose an image mode that encompasses the entire sample (1600x1200 seemed fine for the 0.5x telecentric lens for the compression samples).

(vii) Record the sample cross-section (both sides, top and bottom) with an appropriate telecentric lens for area determination. (The second/macro camera can be conveniently utilized for this by running AVT Smartview on that camera.)

(viii) Run the AVT Smartview software for the coaxial lens (in the first computer) (Note this software and the C-based shot-taking binary called by python scripts do not work at the same time.)

(ix) Make sure that the camera is in the maximum resolution (5 Megapixel) F7 mode through the settings tab.

(x) Determine the limits of the scan area and find a reference feature (such as a pronounced grain's corner) at the corner of the middle image of the scan (this is by convention). This stage includes choosing the scan grid with number of columns and rows as well as the grid spacing. The neighboring images are supposed to slightly overlap each other. Put these settings in the scan code.

(xi) At this point, with the reference feature at the corner, enter the center coordinate of the middle image into the scan code.

(xii) Adjust the coaxial lighting level of the micro-imaging camera; never disturb this level through the experiment. Target high levels of illumination for small shutter speeds since this will protect against blurring of the images with the stage vibration.

(xiii) In the AVT Smartview software, let the micro-imaging camera's shutter auto-adjust for mean image brightness and then fix this value throughout the experiment.

(xiv) Close the AVT Smartview software.

(xv) Run the rough focusing code from the python script (at the coordinate of the first grid point).

(xvi) Run a preliminary YZ scan with fine focusing requested at every grid point.

The introduction of the speckle pattern entails the following details:

(i) Form a coarse pattern in the side of the sample for the macroscopic strain measurement

(ii) Form a fine pattern in the surface of the sample for the microscopic strain measurement.

(iii) Check the pattern quality (enough speckle pattern)

(iv) If the pattern is not enough, form again until it is sufficient.

(v) Clean the optical element including detector face, lens face etc.

(vi) If it is sufficient, run the AVT Smartview software for the coaxial lens (in the first computer)

(vii) Make the sample surface perpendicular to the camera axis. (Rotate the bottom compression rod to achieve this.) To confirm make Y scans (or the first row of a YZ scan) and check the difference between in-focus X values of the leftmost and rightmost images. From an image to its neighbor, in-focus X should not vary by more than half the depth of focus of the camera. A square sample surface is crucial

(viii) Find the reference feature that is determined before.

(ix) Enter the center coordinate of the middle image into the code that you observe at this point with the reference feature at the corner.

(x) Let shutter auto adjust for mean image brightness and then fix its value.

(xi) Close the AVT Smartview software.

(xii) Run the rough focusing code from the python script (at the coordinate of the first grid point).

(xiii) Run a preliminary YZ scan with fine focusing requested at every grid point.

And finally, the following steps are conducted just before the first load of the experiment:

(i) Clean the optical element including detector face, lens face etc.

(ii) Apply grease to the compression platens.

(iii) Place the sample in the middle of the platen.

(iv) Check the cable, screws, and the platen ring for properness.

(v) Run the AVT Smartview software.

(vi) Make the sample surface perpendicular to the camera axis. (Rotate the bottom compression rod to achieve this.) To confirm make Y scans (or the first row of a YZ scan) and check the difference between in-focus X values of the leftmost and rightmost images. From an image to its neighbor, in-focus X should not vary by more than half the depth of focus of the camera. A square sample surface is crucial for problem-free fine focusing of the consecutive images in the scan grid.

(vii) Find the reference feature that is determined before.

(viii) Enter the center coordinate of the middle image into the code that you observe at this point with the reference feature at the corner.

(ix) Let shutter auto adjust for mean image brightness and then fix its value.

(x) Locate and adjust the second camera for macroscopic measurement with a telecentric lens on. Make a specific directory for these images which will be evaluated at run time.

(xi) Adjust the load in the displacement control (0.001 precision)

(xii) Set the ramp duration to 10s

For the nth load:

(xiii) Adjust the load to the nth level in displacement control

(xiv) Take the macroscopic picture of the sample

(xv) Run the AVT camera (AVT camera and the code don’t work at the same time)

(xvi) Locate the reference feature to the specific corner of the center image and enter the center/image coordinate into the python script

(xvii) Fix the shutter

(xviii) Close the AVT camera

(xix) Run the rough focus code (in the first grid point)

(xx) Run the YZ scan with focus adjustment

4.3.2. Speckle Pattern

As it is mentioned in Section 2.1.4, a mechanism is developed to obtain the appropriate speckle pattern for the desired length scale. Figure 4.6, examples of speckle pattern that are formed with this operation are shown. The speckle pattern is applied to the polished and etched surface to see the grain boundary and twin lamellas additionally. Thereby, deformation and twinning steps can be observed visually as well as it can be observed with digital image correlation method.

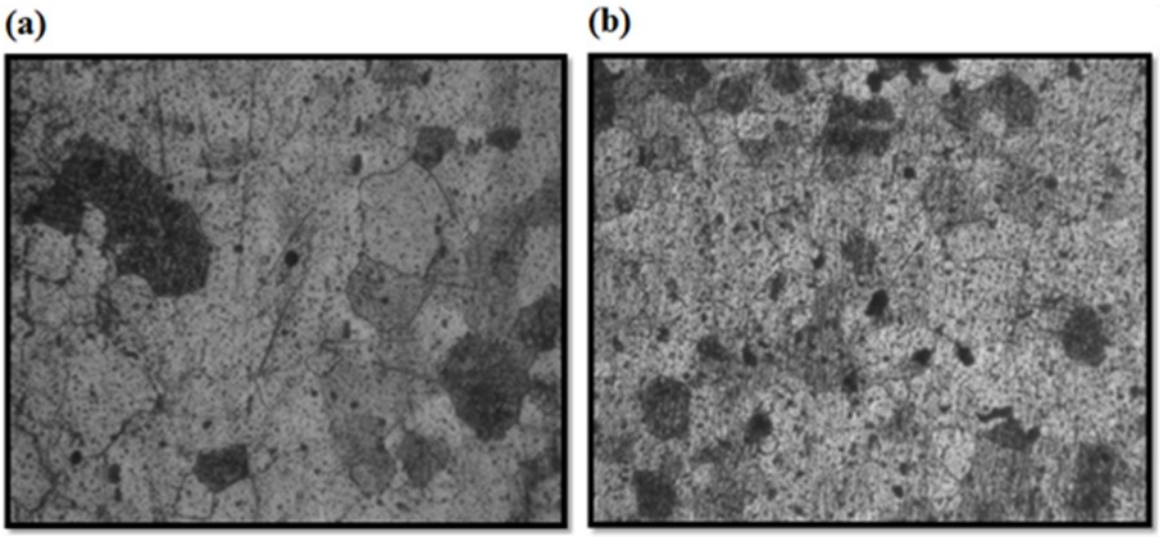

Figure 4.6. A speckle pattern example formed by airbrush with paint.

4.3.3. Multi-scale features of the sample

The experiment is carried out sticking to the procedure that is explained in detail before. Given the serrated and flat nature of the stress strain curve once twinning starts [5,6], the sample is loaded in displacement control so that the deformation can be recorded with fine strain increments.

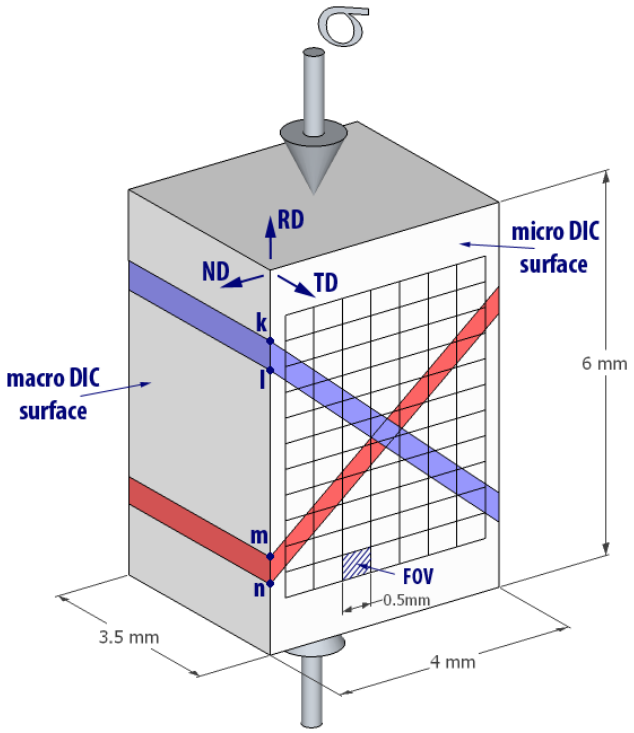

Figure 4.7. Sketch of the compression sample. Two cameras record images from macro-DIC and micro-DIC surfaces *in situ*. The 7x11 grid on the micro-DIC surface corresponds to the images recorded by the micro-DIC [field of view (FOV) shown] camera that is scanned over the surface.

Figure 4.7 summarizes the specifications of the sample used in the experiment. The sample chosen for compression test is an RD sample for which the compression axis is aligned with the RD direction of the plate. The imaging surfaces labeled 'macro-DIC' and 'micro-DIC' are normal to the ND direction and the TD direction, respectively.

The macro-DIC surface images are captured by the macro-scale optical system (details in Section 2.2.3) at each load point. Since the field of view (FOV) of this system is 17 mm (optical resolution 6.8 μm per pixel), it covers the entire sample surface. On the other hand, the micro-DIC surface images are captured by the micro-scale optical system at each load point. The micro DIC surface area is 4x6 mm^2, while the FOV of the micro-scale images are 0.5x0.4 mm^2 providing a resolution of 0.2μm per pixel. To obtain the deformation field from a large area of the surface, the 11 row, 7 column (3x4.4 mm^2) grid

shown in Figure 4.7 has been scanned using the area scan and autofocus codes. The parameters used in the macro-DIC analysis are shown in Table 4.1.

Table 4.1. Parameters of the micro-DIC analysis.

Patch size	61x61 pixels
Distance of the grid point (center point of patch the patch)	10 pixels
Number of grid points per microDIC frame	210x170
Coarse search size	81x81 pixels

Figure 4.8 shows the loading regimen and the stress-strain diagram of the sample obtained from the macro-DIC surface. During the experiment, the sample is loaded up to 156 MPa and unloaded 4 times at different points of plastic deformation.

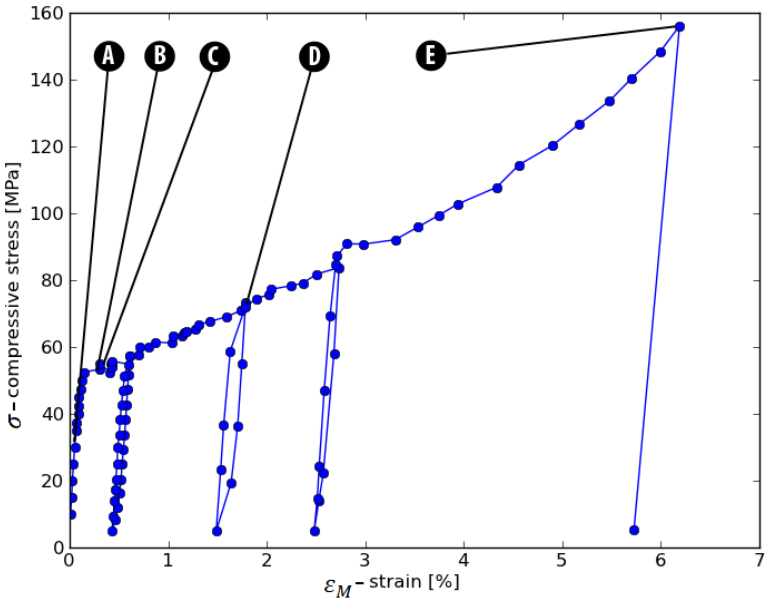

Figure 4.8. Stress - macroscopic strain diagram of the RD sample recorded in the experiment that contains four unloads (Points A-E are specified for further reference.).

ε_M represents the macroscopic strain ε_{yy} measured from the macro-DIC surface. One can discern the occasional serrations (abrupt stress drops) particularly in the span until the second unload. Consequently, in this thesis, ε_M points are used for labeling the loading stage of the images instead of load points or stress points which are not monotonic.

Before examining the DIC analysis results of the macro-DIC and the micro-DIC surfaces, a region is chosen from the micro-DIC surface for a visual description of the deformation steps at the crystallite level (Figure 4.9).

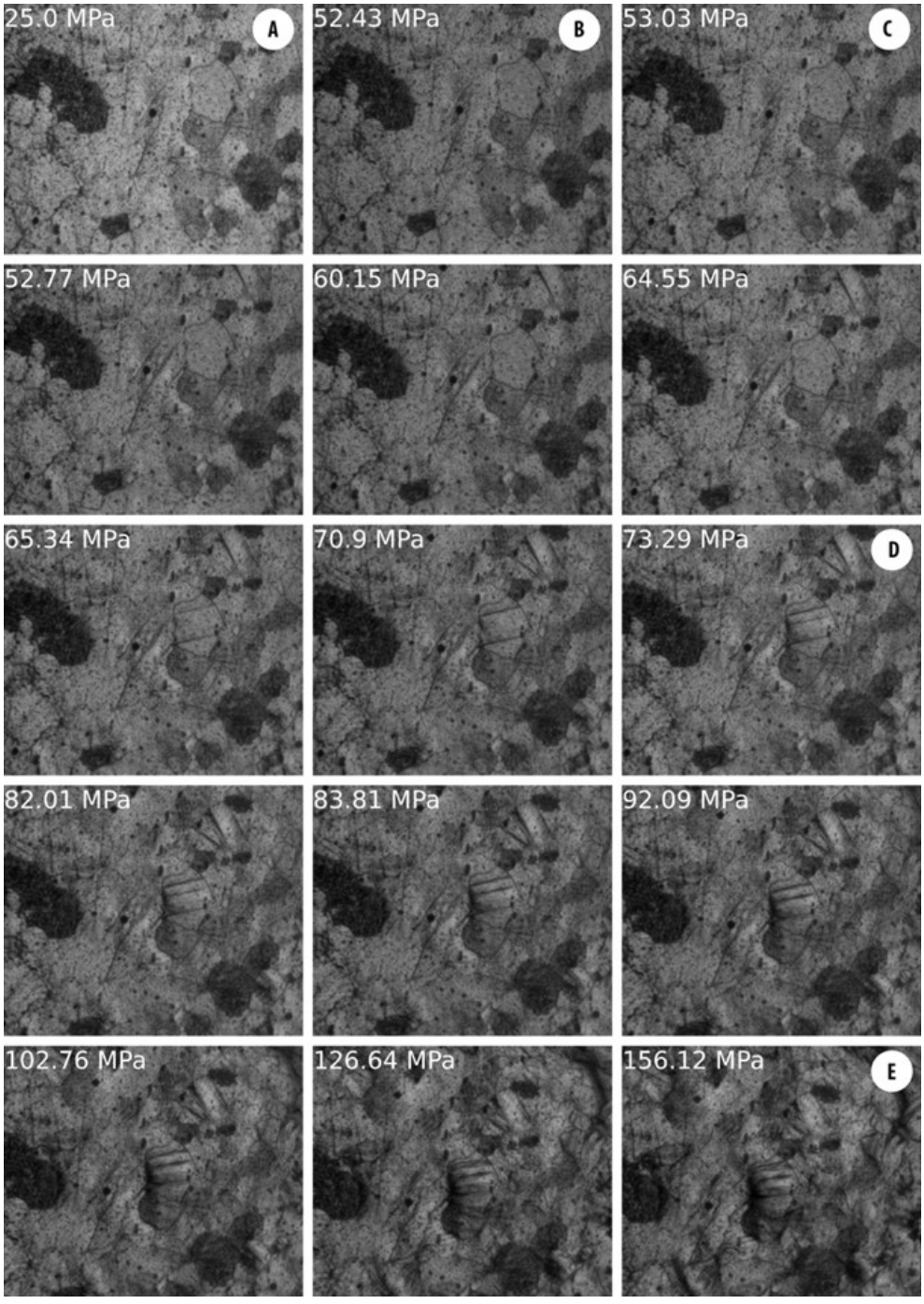

Figure 4.9. DIC Images captured from a small part of the sample that shows the steps of the compression experiment and the sample behavior.

This region (Figure 4.9) includes grains that undergo twinning deformation. All twinning steps can be observed clearly. The loading stage of the images labeled as A, B, C, D, E in Figure 4.9 are marked with the same letters in Figure 4.8. Moreover, the surface topography is altered significantly due to deformation processes that include twinning, as ε_M is increased. The DIC analysis does not work where the topography is altered since the characteristic pattern tracked by DIC gets modified. In subsequent figures, where the DIC analyses are shown, it is seen that the DIC tracking is invalidated particularly in the twin regions. While losing points from the deformation map is clearly undesirable; on the bright side, the invalidated analysis points typically provide an automatic mapping of the twin regions.

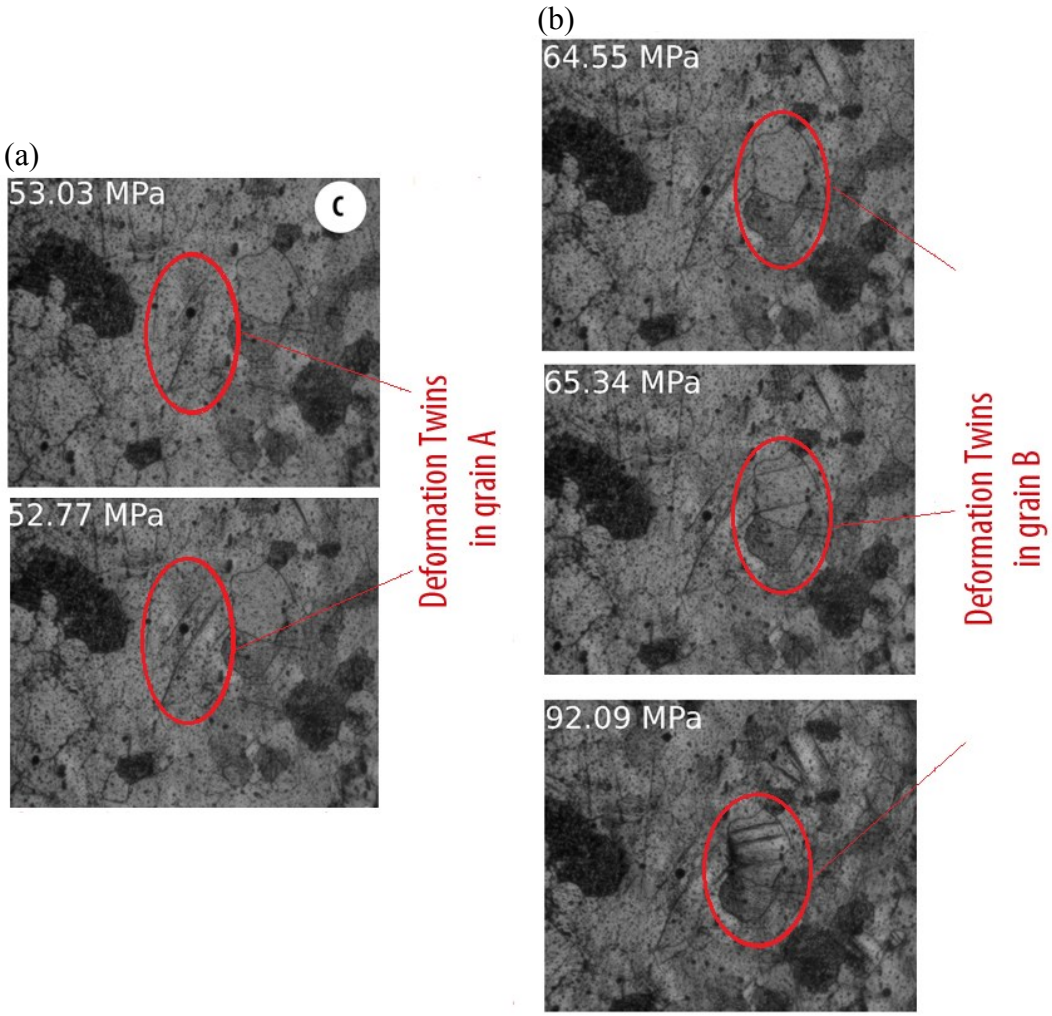

Figure 4.10. Collaborative twin activity in the region of interest of Figure 4.9.

Figure 4.10 is formed categorizing some of the images in Figure 4.9 highlighting the collaborative nature of the twin formation. Formation of a twin in grain A that is presented in Figure 4.10a triggers the neighbor grain B to twin (Figure 4.10b). Then, other twin bands appear and grow in grain(B) as load is increased.

4.3.4. Overall deformation of the sample with adiabatic shear bands

Figure 4.11 shows the 11x7 combination images obtained from the micro-DIC surface at different ε_M points, overlaid with vector plots (red) of the displacement vectors. These displacement vectors are the raw results of the DIC analysis. Since, the vectors are plotted for every analysis points, they appear as red regions when plotted at this scale. In this figure, to highlight the deformation pattern, rigid body displacements (average displacement in each frame) is subtracted from the displacement field of each frame.

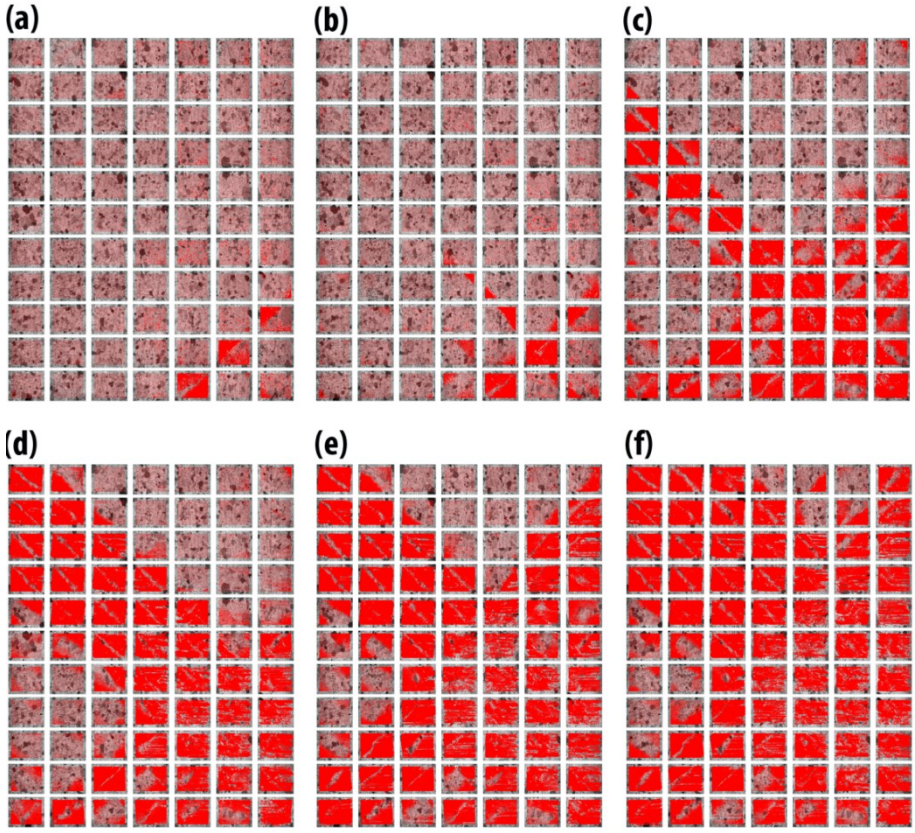

Figure 4.11. 7x11 combination images at different ε_M points. ε_M values in images are respectively, (a) 0.12 %, (b) 0.14 %, (c) 0.28 %, (d) 0.44 %, (e) 0.46%, (f) 0.47%.

Consequently, the orientation of the zero-displacement lines describes the mode of deformation. For example, if the lines were horizontal (perpendicular to the loading axes), it would indicate a homogeneous compressive deformation. The $\pm 45°$ zero-displacement lines observed in Figure 4.11, however, indicate dominant shear processes at these orientations. One can also observe that these 'shear bands' emerge and grow heterogeneously. This means that the deformation occurs locally in the sample (some region of the sample is deformed when others don't).

The heterogeneous deformation can be observed between the ε_M value of 0.12 % and 0.47 % in Figure 4.11. The inhomogeneity of the sample can be proven using the DIC results on the macro-DIC surface as well. Displacement maps of the five ε_M points labeled A-E in Figure 4.8 are detailed in Figure 4.12. The linearity of these maps corresponds to homogeneous deformation. At early loads, when ε_M is under 0.1%, the deformation is linear. At this strain rate, the material is still in the elastic region. When ε_M rises from 0.14 % to 0.28 %, linearity ceases and the deformation is concentrated in a region. This signifies the heterogeneous deformation in the sample. After ε_M is reached to 1.8 %, and in part the plastic deformation seems to have homogenized on the surface.

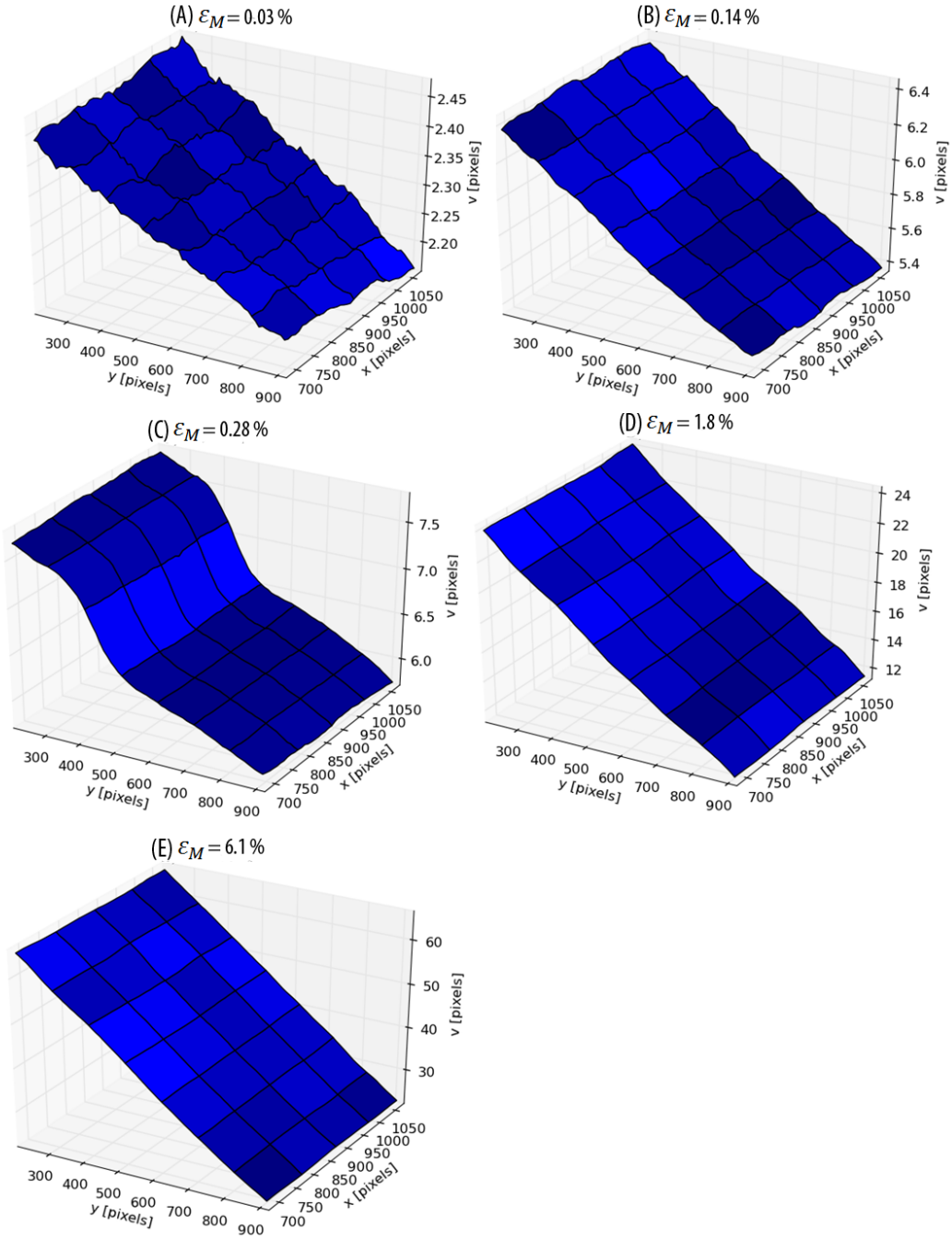

Figure 4.12. Displacement maps of the macro-DIC surface at selected load points A-E shown in Figure 4.8.

To obtain a better idea about the sample behavior, the raw displacement results of the DIC analysis are differentiated to yield infinitesimal strains/rotationε_{xx}, ε_{yy}, ω, ε_{xy} via,

$$\varepsilon_{ij} = \frac{1}{2}\left(\frac{\partial u_i}{\partial x_j} + \frac{\partial u_j}{\partial x_i}\right) \tag{4.1}$$

$$\omega_{ij} = \frac{1}{2}\left(\frac{\partial u_i}{\partial x_j} - \frac{\partial u_j}{\partial x_i}\right) \tag{4.2}$$

In the numerical differentiation over the grid, the central difference formula is used:

$$f'(x) \approx \frac{f(x+h)-f(x-h)}{2h} \tag{4.3}$$

The homogeneous elastic deformation of compression sample obeys

$$\varepsilon_{yy} = -\nu\varepsilon_{xx}, \qquad \omega_{xy} = 0, \qquad \varepsilon_{xy} = 0 \quad . \tag{4.4}$$

where ω is the infinitesimal rotation in the x-y plane. However, results obtained from the micro-DIC analysis for this experiment is typically quite different from this expected behavior.

The experimental result, in most regions, nearly obey

$$\varepsilon_{yy} = -\varepsilon_{xx}, \quad \omega_{xy} = \varepsilon_{yy} \text{ or } \omega_{xy} = \varepsilon_{xx} \quad , \quad \varepsilon_{xy} = 0 \tag{4.5}$$

in regions that appear to be adiabatic shear bands. To reach an understanding, the kinematics of the simple shear process is considered:

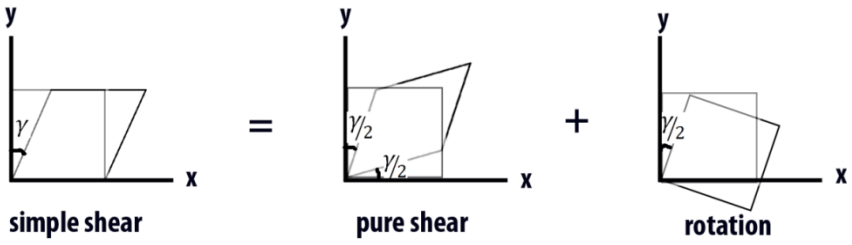

Figure 4.13. A sketch showing simple shear as a superposition of pure shear and rigid body rotation.

One can recall at this point that all plasticity processes are fundamentally simple shear processes be it dislocation slip or twinning. For the simple shear deformation sketched in Figure 4.13, the matrix of deformation gradients e_{ij} is given by

$$e_{ij} = \begin{bmatrix} \frac{\partial u}{\partial x} & \frac{\partial u}{\partial y} \\ \frac{\partial v}{\partial x} & \frac{\partial v}{\partial y} \end{bmatrix} = \begin{bmatrix} 0 & \gamma \\ 0 & 0 \end{bmatrix} \tag{4.6}$$

where γ is the simple shear strain. Deformation gradient is composed of infinitesimal strain and rotation as follows:

$$e_{ij} = \frac{1}{2}(e_{ij} + e_{ji}) + \frac{1}{2}(e_{ij} - e_{ji}) \tag{4.7}$$

$$e_{ij} = \varepsilon_{ij} + w_{ij} \tag{4.8}$$

Using Equations 4.7, 4.8 for the simple shear case, the in-plane components of ε_{ij} and w_{ij} are found as;

$$[\varepsilon_{ij}] = \frac{1}{2}\left[\begin{bmatrix} 0 & \gamma \\ 0 & 0 \end{bmatrix} + \begin{bmatrix} 0 & 0 \\ \gamma & 0 \end{bmatrix}\right] = \begin{bmatrix} 0 & \frac{\gamma}{2} \\ \frac{\gamma}{2} & 0 \end{bmatrix} \tag{4.9}$$

$$[\omega_{ij}] = \frac{1}{2}\left[\begin{bmatrix} 0 & \gamma \\ 0 & 0 \end{bmatrix} - \begin{bmatrix} 0 & 0 \\ \gamma & 0 \end{bmatrix}\right] = \begin{bmatrix} 0 & \frac{\gamma}{2} \\ -\frac{\gamma}{2} & 0 \end{bmatrix} \tag{4.10}$$

Equations 4.9, 4.10 yield pure shear strains and simple shear rotation whose sum yield the simple shear deformation as sketched in Figure 4.13.

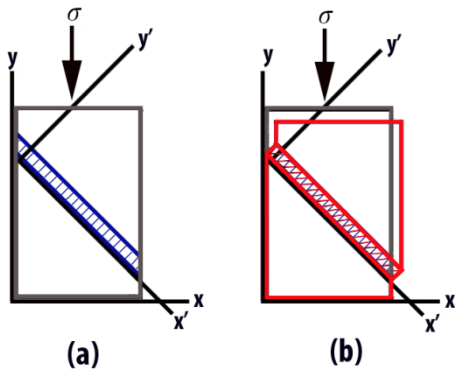

Figure 4.14. A sketch of a dominant macroscopic shear band at a 45° angle with respect to the compression axis.

However, in this experiment, the simple shear phenomenon occurs 45° away from the loading axes (consistent with the maximum shear orientation of a uniaxial test). In Figure 4.14, the deformation of the sample upon the formation of a macroscopic simple shear band at this orientation is sketched. The coordinate system (x', y') is aligned with the shear band. Following the change of basis to the (x, y) sample coordinate system

$$[\varepsilon] = [R][\varepsilon'][R^T] = \begin{bmatrix} \cos 45 & \sin 45 \\ -\sin 45 & \cos 45 \end{bmatrix} \begin{bmatrix} 0 & \frac{\gamma}{2} \\ \frac{\gamma}{2} & 0 \end{bmatrix} \begin{bmatrix} \cos 45 & -\sin 45 \\ \sin 45 & \cos 45 \end{bmatrix} = \begin{bmatrix} \frac{\gamma}{2} & 0 \\ 0 & -\frac{\gamma}{2} \end{bmatrix} \quad (4.11)$$

$$[\omega] = [R][\omega'][R^T] = \begin{bmatrix} \cos 45 & \sin 45 \\ -\sin 45 & \cos 45 \end{bmatrix} \begin{bmatrix} 0 & \frac{\gamma}{2} \\ -\frac{\gamma}{2} & 0 \end{bmatrix} \begin{bmatrix} \cos 45 & -\sin 45 \\ \sin 45 & \cos 45 \end{bmatrix} = \begin{bmatrix} 0 & \frac{\gamma}{2} \\ -\frac{\gamma}{2} & 0 \end{bmatrix} \quad (4.12)$$

So the simple shear aligned with the loading axes can be found by summing the Equations 4.11 and 4.12;

$$\begin{bmatrix} \frac{\gamma}{2} & 0 \\ 0 & -\frac{\gamma}{2} \end{bmatrix} + \begin{bmatrix} 0 & \frac{\gamma}{2} \\ -\frac{\gamma}{2} & 0 \end{bmatrix} = \begin{bmatrix} \frac{\gamma}{2} & \frac{\gamma}{2} \\ -\frac{\gamma}{2} & -\frac{\gamma}{2} \end{bmatrix} \quad (4.13)$$

From Equation 4.13, it is seen that $\varepsilon_{xx} = \frac{\gamma}{2}$, $\varepsilon_{yy} = -\frac{\gamma}{2}$, $\omega_{xy} = \left|\frac{\gamma}{2}\right|$, $\varepsilon_{xy} = 0$ as in the experiment result. The infinitesimal rotation ω_{xy} is coordinate independent in the plane ($\omega_{xy} = \omega_{x'y'}$), which explains the use ω without indices here.

In this study, contour plots of ε_{xx}, ε_{yy}, ω, ε_{xy} are presented to show the morphology of the deformation with respect to grain structure. To follow the progress of the deformation map for the micro-DIC surface, ω is favored as the contour plot parameter. The main reason behind this choice is that ω changes sign according to the sense of the $\pm 45°$ shear band providing contrast in a region of heavy shear activity. Figure 4.15 contains a sketch to show the connection between the direction of the shear band and ω.

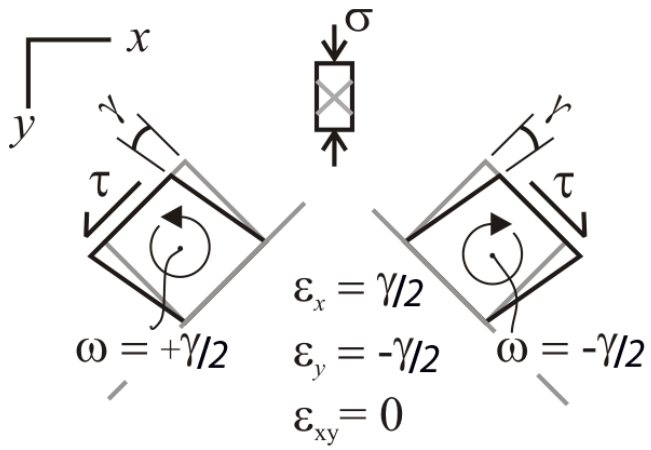

Figure 4.15. Infinitesmal strains in the x-y coordinate system and infinitesimal rotation for the $\pm 45°$ shear bands.

Out of the two conjugate shear band families shown in Figure 4.7, the red one corresponds to the shear sense shown on the left in Figure 4.15 and a positive rotation ω results. The opposite argument is valid for the blue band in Figure 4.7, corresponding to the shear sense on the right in Figure 4.15 causing a negative rotation ω. Assigning red tones for positive ω and blue tones for negative ω in the color map of the contour plots then, clearly, yields an auto confirmation of the $\pm 45°$ shear processes as well as their senses. This is demonstrated clearly in the combination contour plots that put together the results of all micro-DIC frames in the 11x7 grid (Figure 4.16). The formation and growth of the two conjugate adiabatic shear bands as the load is increased, is clearly visible.

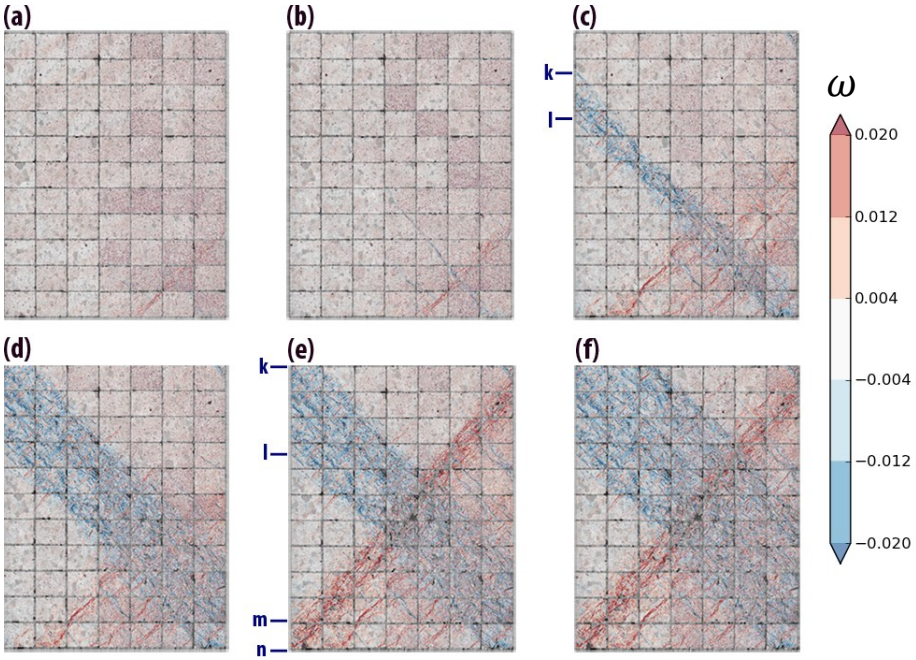

Figure 4.16. ω graphs of the 7x11 images taken from the micro-DIC surface which belongs to different ε_M points, (a) 0.12 %, (b) 0.14 %, (c) 0.28 %, (d) 0.44 %, (e) 0.46%, (f) 0.47%.

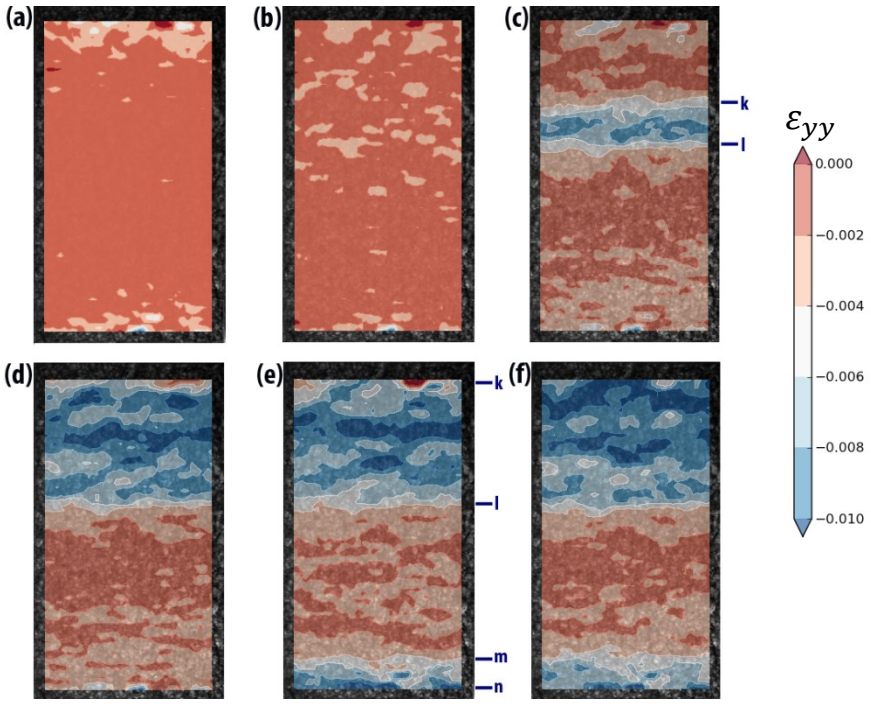

Figure 4.17. ε_{yy} graphs images taken from the macro-DIC surface which belongs to different ε_M points, (a) 0.12 %, (b) 0.14 %, (c) 0.28 %, (d) 0.44 %, (e) 0.46%, (f) 0.47%.

Figure 4.16 shows the ω graph of the combination images belonging to the micro-DIC surface sketched in Figure 4.7. Complimentarily, Figure 4.17 indicates the ε_{yy} graph of the images which belongs to the macro-DIC surface in Figure 4.7. In both figures, the images are labeled (a) to (f). Images labeled with the same letter correspond to the same loading point ε_M which increases monotonically from (a) to (f). Figure 4.16 and Figure 4.17 show the progress of the deformation in the micro-DIC and macro-DIC surface, respectively.

From Figure 4.16, the domination of the two conjugate shear bands throughout the sample surface can be observed. As mentioned before, this causes deformation heterogeneity in the sample surface. However, the heterogeneity and the conjugate shear bands do not occur only in the micro-DIC surface. They proceed along the volume of the sample. To show that shear banding here is a volumetric phenomenon, points *k, l, m* and *n* are indicated in both Figure 4.16 and Figure 4.17. In Figure 4.16c, when ε_M reaches 0.28%, the blue shear band forms and hits the left side of the micro-DIC surface between points *k* and *l*. At the same strain level, in Figure 4.17c, the strain is locally increased between the same points *k* and *l*. Here, the 3-D picture can be realized in Figure 4.7 as the blue shear band with *k* and *l* indicated. As ε_M gets to the 0.47% strain level, in Figure 4.16e, the blue shear band widens and the *k-l* gap is extended. Further, at this level, the conjugate adiabatic shear band (red) hit the left side of the surface between points *m* and *n*. At the same strain level, in Figure 4.17e, the strain is concentrated between *k* and *l* and the *m* and *n* in agreement with Figure 4.16. The red shear band can also be seen in Figure 4.7. This strongly corroborates that the shear bands extend through the sample volume and are not constrained to the surface.

The orientation of the shear bands is highly related with the texture of the material. Padilla et al [19] investigated the relation between the local texture and the heterogeneity in zirconium alloy. They found that the strain heterogeneity highly depends on the texture of the material, especially in micro scale. Since the magnesium plate used in this experiment has strong textured, the behavior of the sample is changed according to the direction of the plate. Since the grains are mostly oriented in the form of their *c* axes are aligned with the

ND, the twin occurs shaped like horizontal line in ND face while they occur shaped like inclined line in TD face.

It can be clearly seen that the strain is high where the macroscopic shear bands occur. However, contour plots hardly convey exact numbers and to quantify rotation and strain, results are plotted over selected lines in the micro-DIC surface.

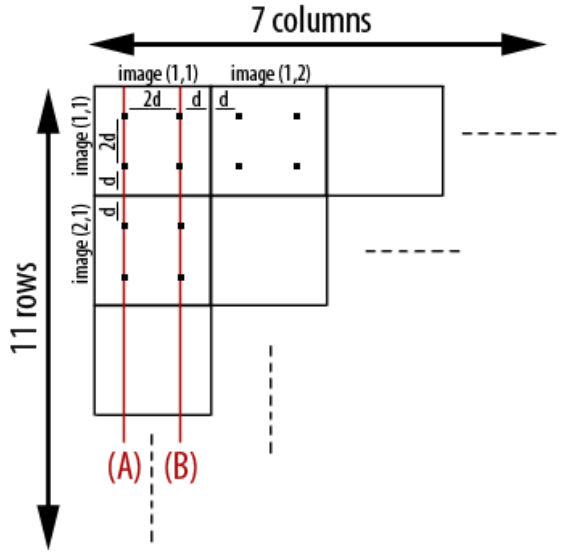

Figure 4.18. Description of the average strain grid and data points used in Figure 4.19.

For this purpose, average strains are considered that are calculated by designating four regions in each micro-DIC frame. The center point distances of these regions are selected equal among all micro-DIC frames, designated as *2d* in Figure 4.18. A strain value is averaged from each region (whose size is nearly one fourth of the 210x170 frame analysis grid). Taking four strain values instead of one average strain value per frame allows a finer resolution strain plot.

The graphs of Figure 4.19 show average ε_{xx}, ε_{yy}, ω, ε_{xy} variation over two vertical lines (corresponding to parts (A) and part (B)) that fall in the first column of the microDIC image grid [shown in Figure 4.18 and Figure 4.16 with lines labeled (A) and (B)] at ε_M is 0.47 %.

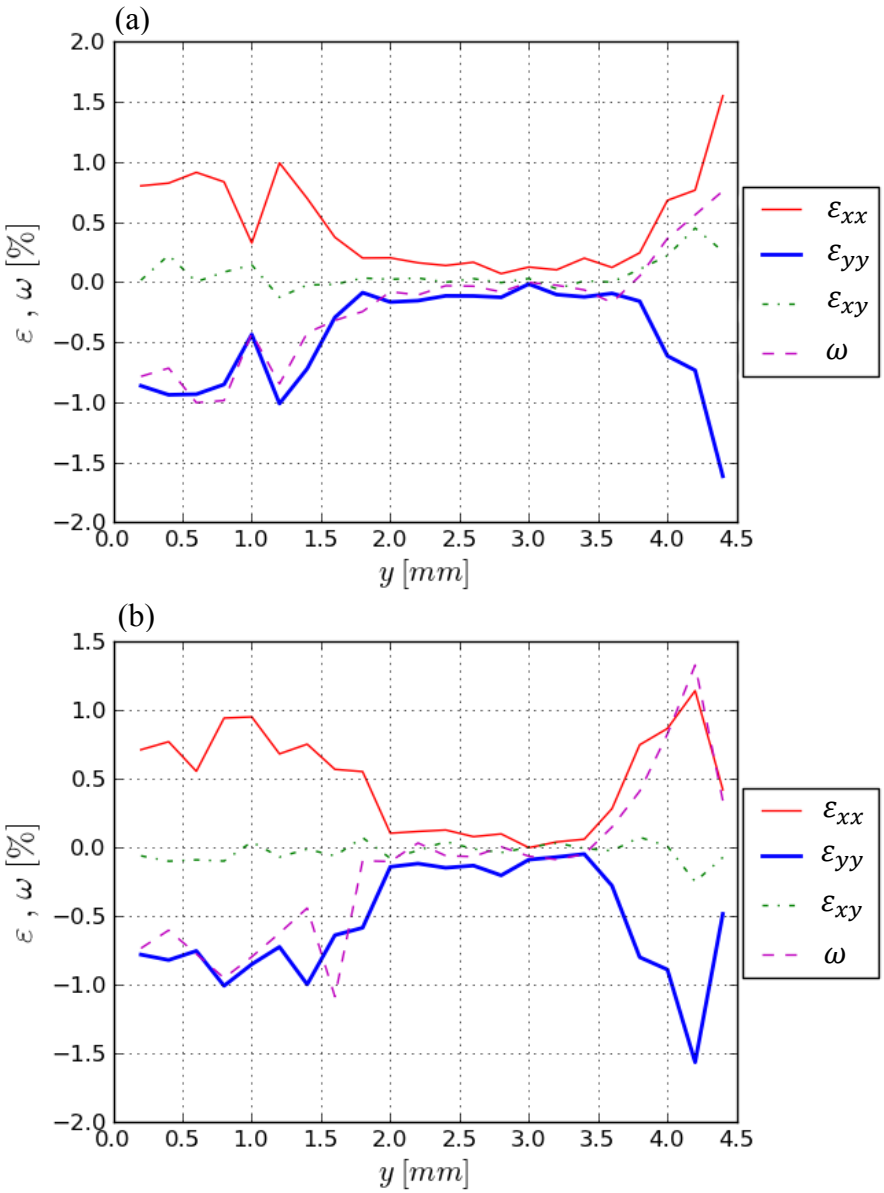

Figure 4.19. ε_{xx}, ε_{yy}, ω, ε_{xy} graphs over the y-axis of the microDIC surface following lines (A) and (B) in Figure 4.18.

In the upper part of the column1 (the vertical y is between 0-1.2 mm) where the shear band occurs, the ε_{xx}, ε_{yy} magnitudes reach approximately 1 %. Since the blue shear band is dominant in these frames, ω is negative as expected. The value of the rotation is the same as the ε_{yy} value. In the middle of the column (the vertical y is between 1.2-3.7 mm) where the shear band does not exist, the strain values are approximately 0.2 %. Strain localization with shear banding is not observed in this zone, so near zero rotation is

observed in this region in Figure 4.19a. In the bottom part of the column (the vertical y is between 3.7-4.5 mm), the strain values ε_{xx}, ε_{yy} again raise to 1% since, now, the conjugate (red) shear band is dominant in this zone. Consequently, ω sense is opposite (positive), and it begins to track ε_{xx}. Column 2 results, shown in Figure 4.19b, exhibit the same general trends. Only difference is that the gap between the two shear band families is smaller as can be physically observed in Figure 4.16.

Invoking the fact that plastic deformation preserves material volume can further shed light on the volumetric deformation of the sample. Since $\varepsilon_{yy} = -\varepsilon_{xx}$ in the simple shear zones, the Poisson's ratio becomes approximately 1. This means, deformation volume is preserved already and the Poisson expansion the in z-direction should be near zero. This fact is indeed apparent in ε_{xx} values of macro-DIC surface since the x-direction of macro-DIC surface coincides with the z-direction of the micro-DIC surface. Figure 4.20 shows the in-plane Poisson's ratio (lateral strain divided by compressive strain) vs. compressive strain of the macro-DIC surface for all steps of the experiment.

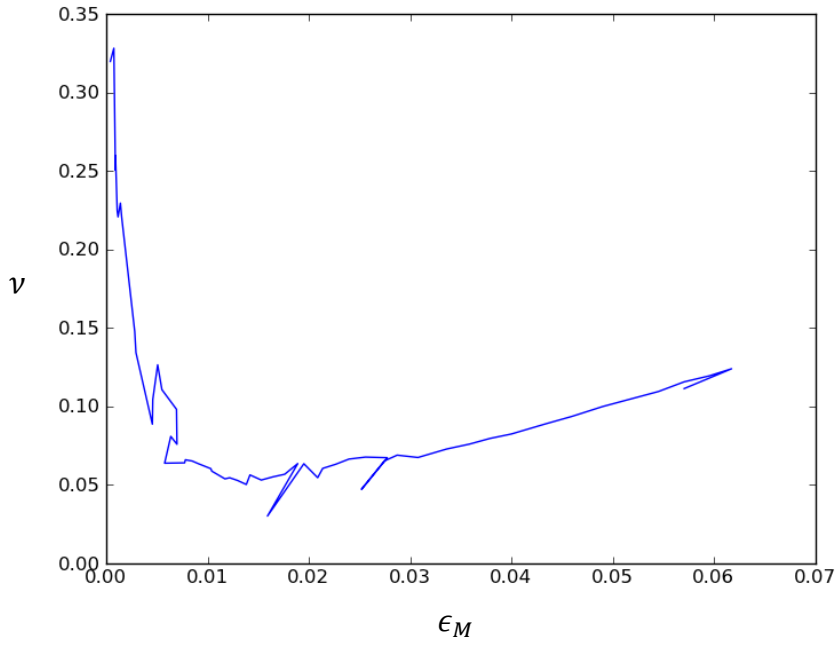

Figure 4.20. Poisson's ratio vs. compressive strain of the macro-DIC surface for the entire experiment (see Figure 4.8).

4.3.5. Crystallite-level (mesoscale) observations

This section provides information by focusing on the results of individual frames in the micro-DIC analysis. Frames are designated with their location in the 11x7 grid with their row and column number.

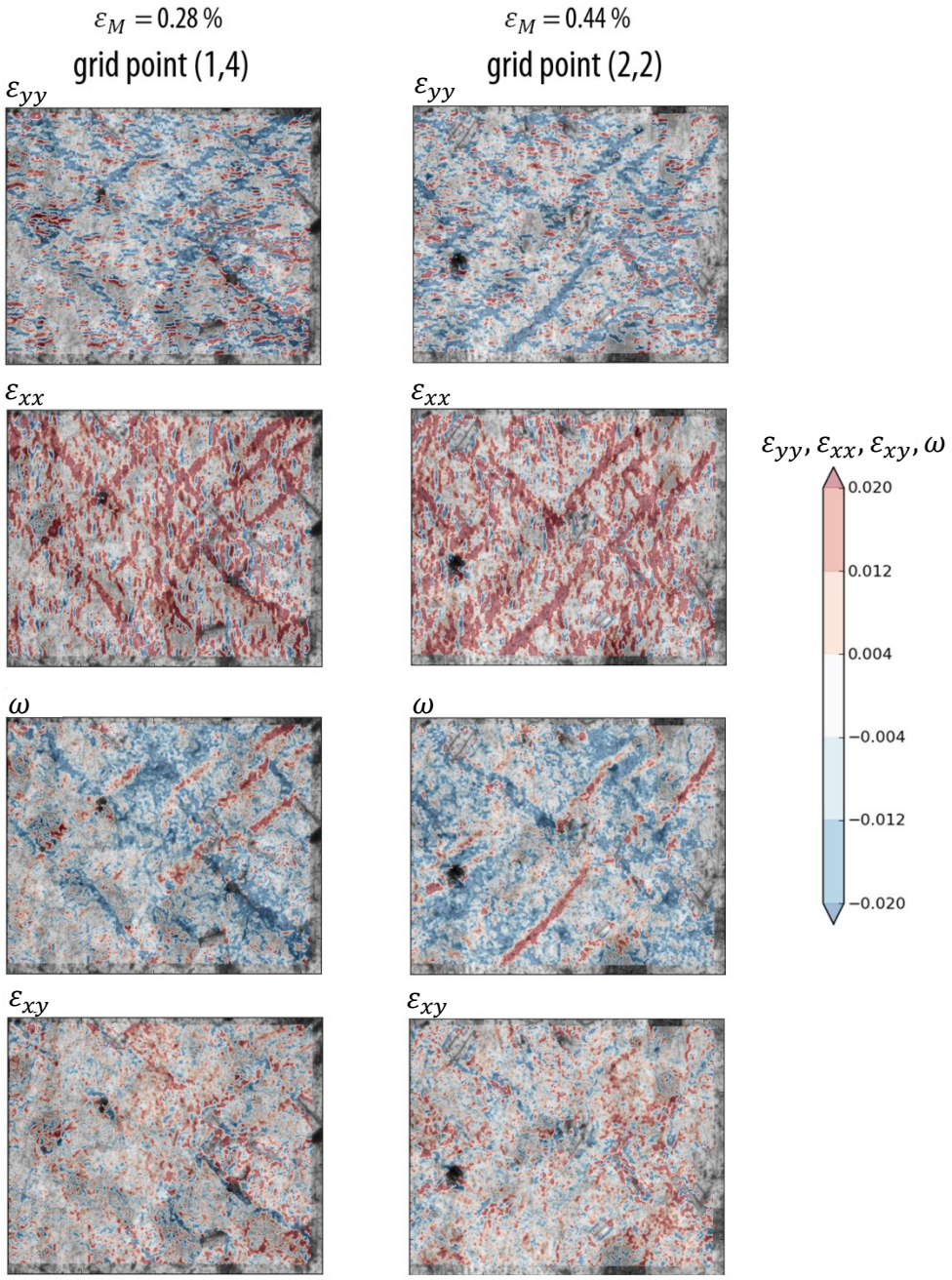

Figure 4.21. ε_{yy}, ε_{xx}, ω, ε_{xy} contour plots of two micro-DIC frames. The plots are overlaid over the deformed microscopic images (grayscale).

ε_{yy}, ε_{xx}, ω, ε_{xy} contour plots of two frames are provided in Figure 4.21. The contour plots in this section are overlaid over the deformed gray-scale images of the frame itself. The first column in this figure belongs to the frame at grid point (1,4) when $\varepsilon_M = 0.28\%$ and the second column is for grid point (2,2) when $\varepsilon_M = 0.44\%$. For these two images, different ε_M points are chosen since the strain localization (shear banding) initiate at different loads.

The strain localization into bands of $\pm 45°$ to the loading axis at the mesoscale has been observed in HCP materials [12,13,19]. As the analyzed regions are reduced from the sample-level to individual micro-DIC frames (the length scale is smaller), a higher level of strain heterogeneity is observed. At lower length scale, the number of $\pm 45°$ conjugate shear bands is dramatically increased, so the strain distribution becomes more heterogeneous. Efstathiou *et al.* and Padialla *et al.* indicated that the strain localization resolved better as the length scale lower so greater heterogeneity is observed in that length scale

These graphs also show why ω is desirable as the plotting variable. The shear bands can be recognized in ε_{xx} and ε_{yy} plots as well; however, the sense of these strains does not distinguish between the two families of the shear bands shown Figure 4.15. So all the shear bands appear blue, since ε_{yy} is negative. Similarly, all the shear bands appear red in ε_{xx} plots, since ε_{xx} is positive.

In Figure 4.22, ω contour plots of two frames at grid points (7,4) and (6,5) are shown as the deformation evolves with increasing load (ε_M). For frame (7,4), the blue shear band begins to form at ε_M is 0.12 % which goes through the circled region in the image. When ε_M reaches 0.28 %, the analysis in this region loses validity and a twin appears in this part of the shear band. Recall DIC analyses lose validity due to the surface steps created by the twin formation and resulting modification of the DIC pattern. When ε_M gets to 0.46 % strain value, twin is formed and grows in another part of the shear band that is encircled in this image.

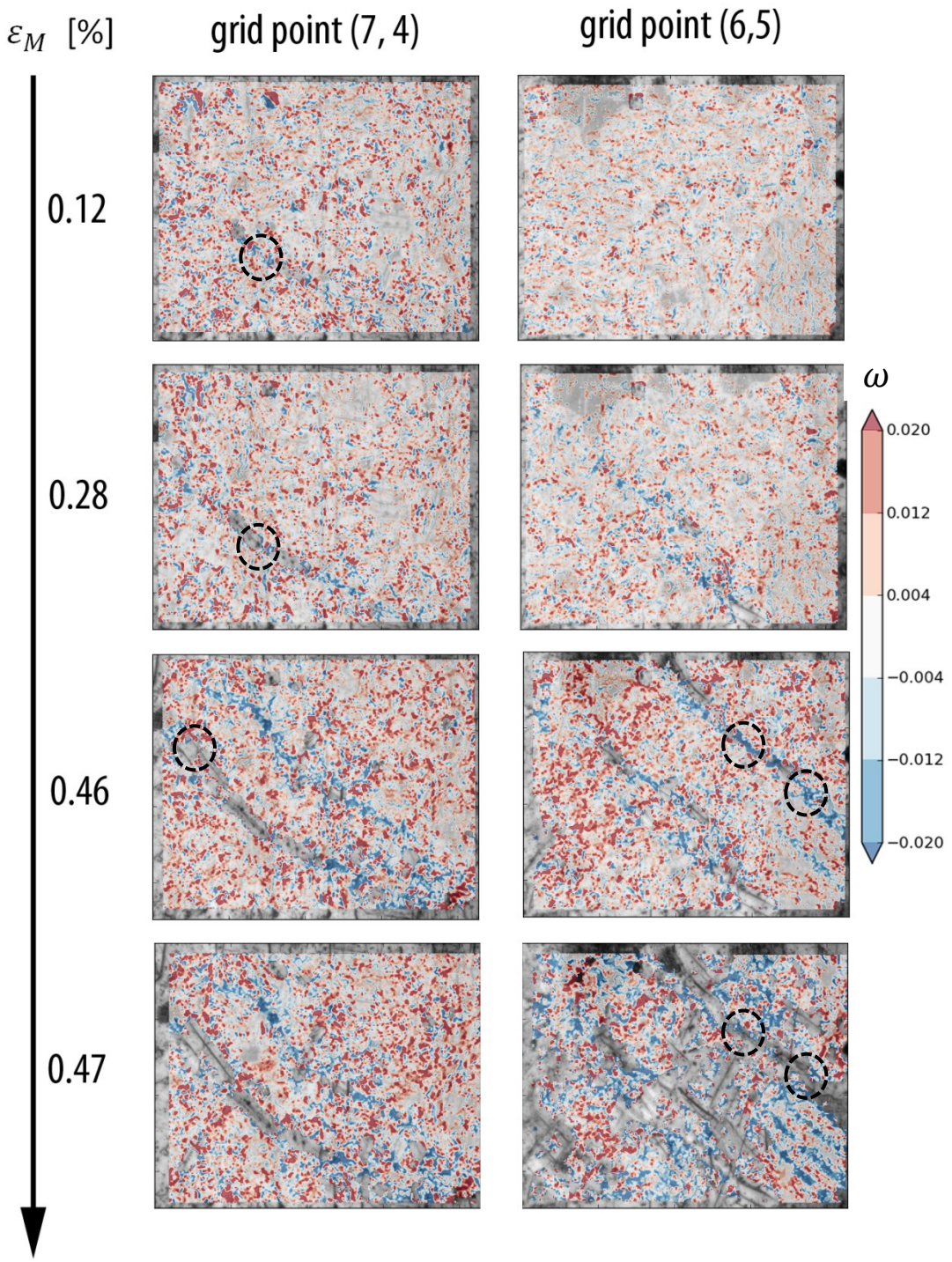

Figure 4.22. Contour plots of infinitesimal rotation evolution (ω) of frames (7,4) and (6,5) with increasing load. The plots are overlaid over the deformed microscopic images (grayscale).

Frame (6,5) leads to similar conclusions. Especially, when ε_M rises from 0.46 % to 0.47 %, twins appear (circled regions for $\varepsilon_M = 0.47$ %) in place of the high strain shear bands (circled blue regions at $\varepsilon_M = 0.46$ %), as the DIC analysis is invalidated. It can be speculated that DIC works reasonably well at the initial stages of the twin, when the deformation it causes does not create a large surface step. This means that, at early stages, the twin might be imperceptible to DIC whose pattern can still be tracked.

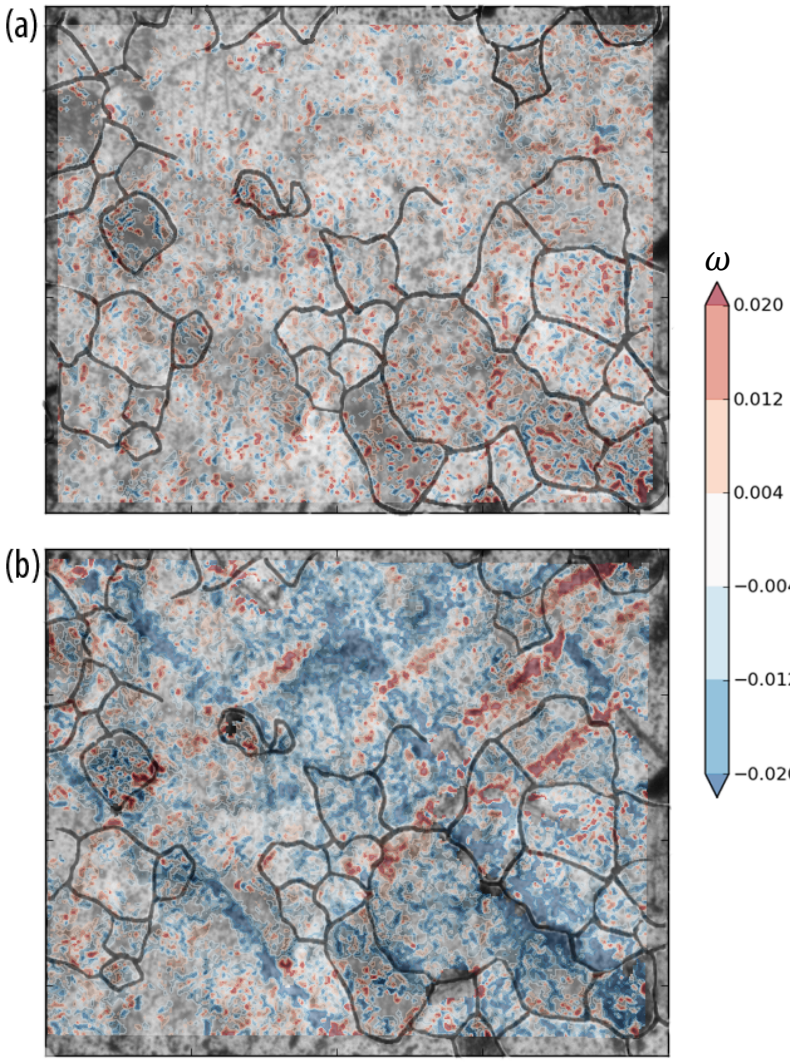

Figure 4.23. Infinitesimal rotation (ω) contour plots of frame at grid point (4,1) at (a) $\varepsilon_M = 0.14$ %, (b) $\varepsilon_M = 0.28$ % . The plots are overlaid over the deformed microscopic images (grayscale) and grain boundaries are traced for clarity.

Figure 4.23 is formed to show that strain localization mostly follows grain boundaries. [12,14,16]. They all pointed out that stain localization appeared mostly near grain boundary and grain boundary triple in the form of $\pm 45°$ shear band to the loading axes. The grain boundaries are traced in Figure 4.23 for further clarity in making this point. Padilla *et al.* [19] stated that the grains of particularly dissimilar orientations and hence dissimilar stiffness, chose to form regions of intense strain among each other instead of satisfying compatibility with their entirety. It might be argued that larger grains (as in this study) will show a higher tendency for strain localization since they would prefer to minimize the strain energy of the large volume of the grains. Typically, the shear bands that inclined $45°$ to the loading direction lie along several grains whose orientations are similar or close to each other.

5. CONCLUSION

Full-field deformation maps in AZ31 magnesium alloy at both macroscopic and microscopic length-scales are measured by *in situ* optical digital image correlation method. Based on these results, the effects of the deformation twinning in this alloy are examined closely.

For this purpose, a compression sample from a hot-rolled plate is acquired whose loading axis of the sample coincides with the rolling direction (RD). The two orthogonal faces of the sample that correspond to the transverse and normal directions in the plate (TD and ND) are imaged *in situ* by the micro-scale and macro-scale optical systems, respectively, during the course of a compression experiment. Consequently, TD face is used for the microscopic DIC analysis and the ND face is used for the macroscopic one. To record data from a large area in the TD face with a microscopic setup, the face is scanned with a positioning setup. This yields an 11x7 connected array of microscopic frames.

The local (crystallite-level) shear bands observed in the contour plots of in-plane infinitesimal rotation coalesce to form macroscopic shear bands on the sample scale. These macroscopic shear bands are clearly visible in the combination graph of the entire grid (11x7) of microscopic frames on the TD face and belong to two conjugate shear band families that are oriented $\pm 45°$ to the loading axis. This indicates a very high level of heterogeneity both at micro and macro scales. The direct consequence of high heterogeneity is that there is no representative volume element at any length scale.

The deformation fields that fall in the shear band zones clearly demonstrate strain and rotation fields expected from a simple shear process. In these zones, contrary to the homogenous strain field of a uniaxially loaded specimen, infinitesimal rotation ω is not zero: It equals ε_{yy} or ε_{xx} depending on the sense of the of $\pm 45°$ shear band. Consequently, such infinitesimal rotation fields provide a confirmation of $\pm 45°$ shear processes and present their senses.

Although DIC is a surface technique, a volumetric picture of the sample deformation is derived from the use of two cameras that image two orthogonal faces of the sample. It is determined that the macroscopic shear bands are volumetric formations. The shear bands in the TD face proceed along the ND face and appear as horizontal sections of strain localization on the macroscopic DIC surface. This orientation of the shear band is highly related to the texture of the material which also reveals itself in the measurement of Poisson's ratios. Accordingly, the plastically hard ND face reveals very small Poisson's ratios (around 0.1) once twinning activity starts which is heavily observed on the TD face with Poisson's rations near 1, the value consistent with the $\pm 45°$ simple shear processes.

It is also determined that the level of local strain heterogeneity is higher at lower length scale. Moreover, $\pm 45°$ shear bands that extend over several grains follow grain boundaries rather than cutting through the grains, an observation commonly supported by literature. This can be explained by differently-oriented neighbors choosing to localize the strain in a small zone among them instead of an overall straining to satisfy compatibility. The DIC analyses suggest that DIC tracking can work well enough at the early stages of twinning. Once surface deformation steps due to twin bands sufficiently alter the DIC pattern, the DIC is invalidated in these regions. On the bright side, this allows an automatic tracking of the twin formation. It is apparent that the zones of very high twin activity match with the zones of very high strain localization, like the merger zone of the conjugate macroscopic shear bands. This is consistent with the visual observation in the microscopic images that twins in a grain trigger twins in the neighbor following the intersection point at the common grain boundary. Thus, twinning appears to play a big role in strain localization.

6. FUTURE WORK

6.1. Photolithography

This method is one of the main production methods in microelectronics. The spackle pattern in the desired scale is designed in the computer. This design can be applied to the surface without any difference, so it is more precise and accurate than the paint method with airbrush.

In photolithography method, desired speckle pattern designed in the computer is processed in a mask. An example of speckle pattern formed by photolithography in the computer is shown in Figure 6.1. On the other side, a resin named photoresist is applied to the sample surface with a desired thickness by spin coaters. The sample with photoresist is placed in machine then the mask is superimposed on the sample. Then the sample is exposed directly to the UV rays. While the region that is exposed to the UV rays become tough to the chemicals, the rest of them stay weak. After this process, the sample is etched with the proper chemicals to be purified from the photoresist that stays weak. So the desired speckle pattern is formed over the sample.

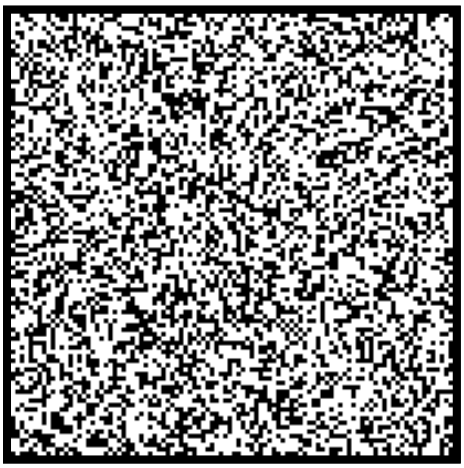

Figure 6.1. A simulation of a photolithograpy pattern formed in computer.

APPENDIX A: EFFECT OF COLOR FILTERS

Color filters have been tested with a typical microscopic image. For all images, shutter speed is allowed to adjust for mean gray value of 125. In this case, the shutter speed is 10 ms for no filter. For blue, cyan, red, green, yellow, magenta filters, the auto-adjusted shutter drop to 129, 31, 18, 78, 14, and 19 ms, respectively.

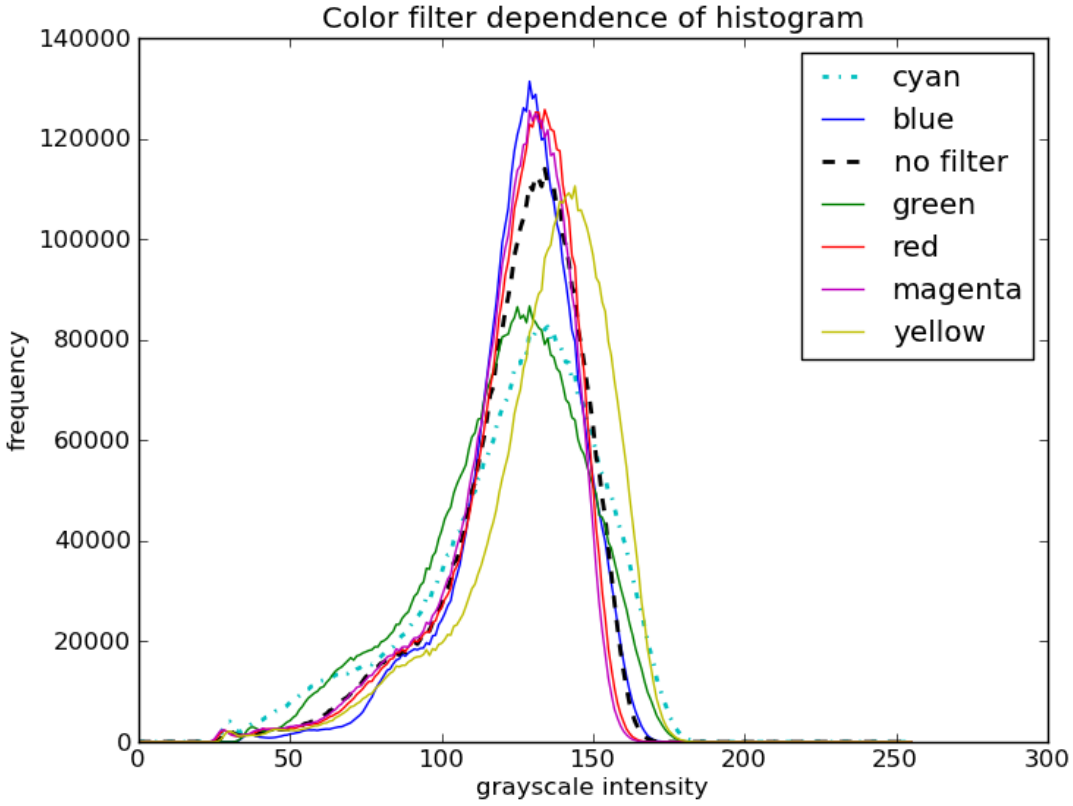

Figure A.1. Frequency-intensity diagram of the color filters that shows intensity distribution and its frequency.

Figure A.1 shows that, cyan filter provides more color contrast with wider dynamic range when compare other filters and no filter. Grayscale intensity range of cyan is more balanced than others. Figure A. 2 shows filtered (b) and unfiltered (a) microstructure photographs.

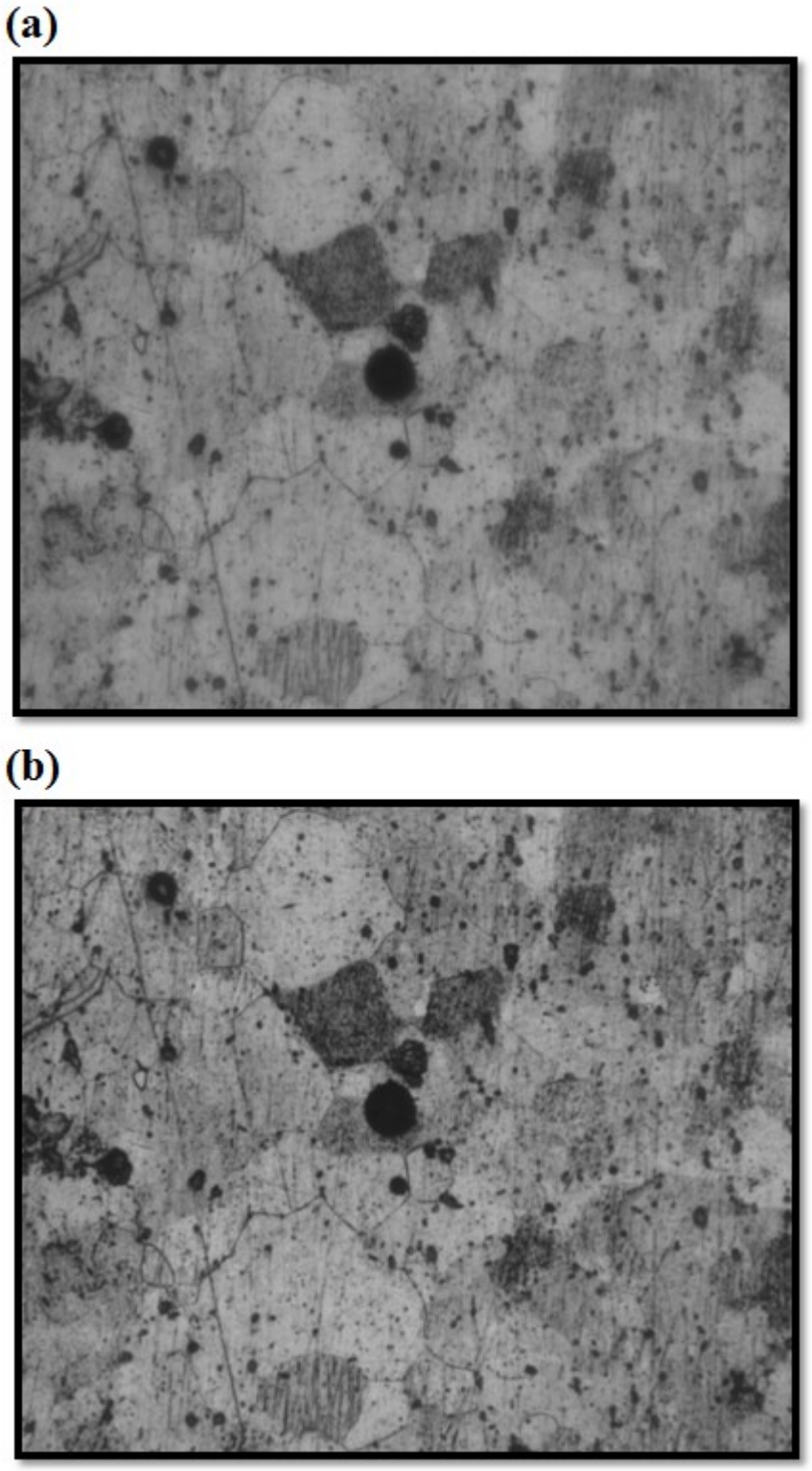

Figure A. 2. (a) Unfiltered and (b) Filteredmicrostructure photographs.

APPENDIX B: STANDART DEVIATION FROM FIXED DISPLACEMENT TESTS

Even for images taken at the same exact location, DIC measurement will entail errors (it will not produce a perfect zero-displacement field). This is due to errors in lighting, detectors and also a minute change in the camera and sample positions at the exact moment of taking the picture due to, say, vibrations. One can also introduce a controlled rigid body motion and evaluate the method. In each case, the sample displacement is evaluated over a regular grid. Since this displacement is physically constant any deviation of displacement over the grid is representative of the minimum error in the DIC procedure. To get a feeling for the best case, an Mg sample has been painted at the macro-scale with the recommended procedure of black speckles over a white basecoat. The observed standard deviation over a statistically significant (25x15) grid is roughly 0.007 pixels for 61x61 pixel patches. For 21x21, 41x41 and 81x81 pixel patches, the standard deviation is 0.02, 0.009 and 0.006 pixels. All this is consistent with the fact that the smaller the patch, the less signature it contains and deviations rise.

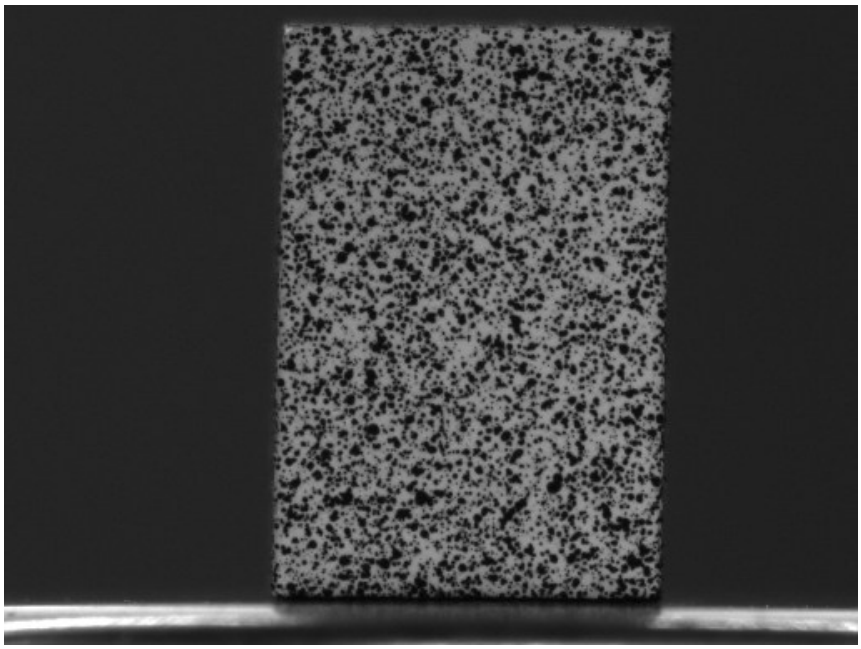

Figure B.1. Vibration analysis based on micro-scale DIC.

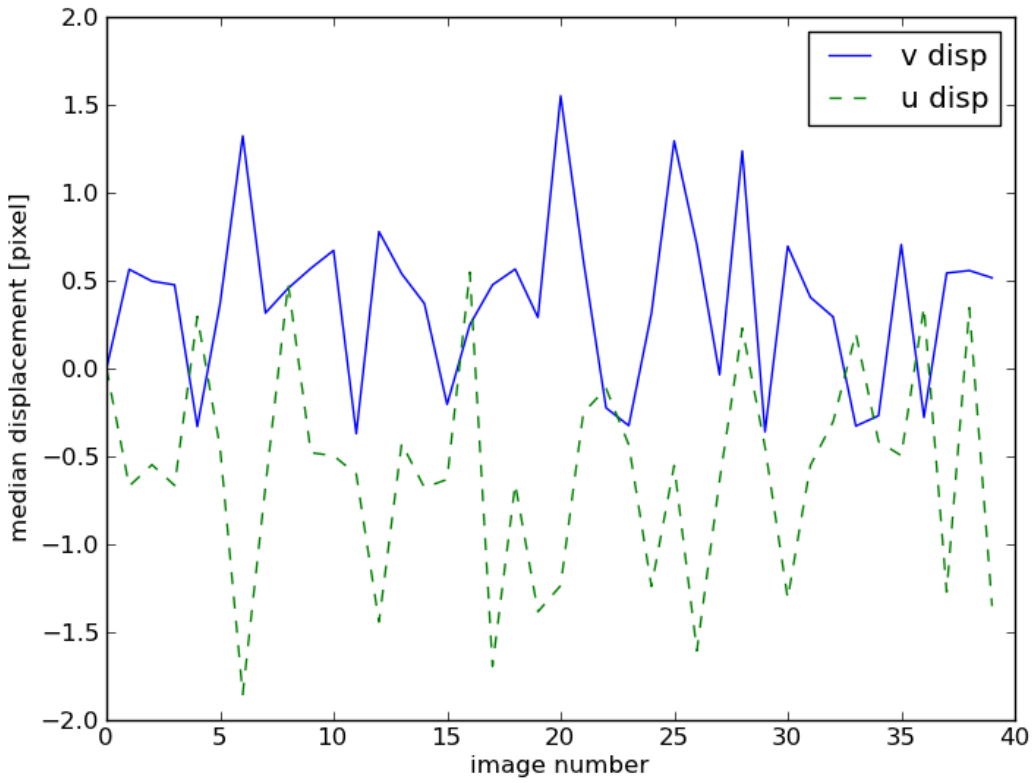

Figure B.2. The median displacement over a 35x27 grid of the 40 images with respect to the first image.

For this study, consecutive 40 pictures were taken with the fastest operation of the singleShot.exe code (which meant every 0.4s). This way, these pictures were taken within 20s, a time interval which is small for any ambient temperature change to take effect. (An ambient temperature change of even 1 ℃ creates pronounced shifts in the tall stage structure that holds the camera.) Figure B.2 shows the median displacement over a 35x27 grid of the 40 images with respect to the first image. The stochastic variation indeed resembles random vibration. The mean of these curves are not really significant, they just have to do with the exact location the first image was taken. Rather, the amplitudes exhibit the level of vibration. Since, maximum amplitude appears to be about 2 pixels, vibration amplitude is about 0.3 micrometers for the 18.2X lens setting. This study is conducted in the original form of the setup and vibration isolation.

REFERENCES

1. Nemat-Nasser, S. and M. Hori, *Micromechanics: Overall Properties of Heterogeneous Materials*, 2 ed., Elsevier, North-Holland, 1999.

2. Roters, F., P. Eisenlohr, T. R. Bieler and D. Raabe, *Crystal Plasticity Finite Element Methods in Materials Science and Engineering*, Wiley-VCH, Weinheim, 2008.

3. Hutchinson, J. W., "Elastic-plastic behaviour of polycrystalline metals and composites", *Proceedings of the Royal Society of London, Series A (Mathematical and Physical Sciences),* Vol. *319*, No. 1537, pp. 247-72, 1970.

4. Hosford, W. F., *The Mechanics of Crystals and Textured Polycrystals*, Oxford University Press, New York, 1993.

5. Hertzberg, R. W., *Deformation and Fracture Mechanics of Engineering Materials* 5ed., John Wiley & Sons, England, 2013.

6. Brown, D. W., S. R. Agnew, M. A. M. Bourke, T. M. Holden, S. C. Vogel and C. N. Tome, "Internal strain and texture evolution during deformation twinning in magnesium", *Materials Science and Engineering A,* Vol. *399*, No. 1-2, pp. 1-12, 2005.

7. Clausen, B., C. N. Tomé, D. W. Brown and S. R. Agnew, "Reorientation and stress relaxation due to twinning: Modeling and experimental characterization for Mg", *Acta Materialia,* Vol. *56*, No. 11, pp. 2456-2468, 2008.

8. Agnew, S. R., D. W. Brown and C. N. Tome, "Validating a polycrystal model for the elastoplastic response of magnesium alloy AZ31 using in situ neutron diffraction", *Acta Materialia,* Vol. *54*, No. 18, pp. 4841-52, 2006.

9. Xu, F., R. A. Holt and M. R. Daymond, "Modeling lattice strain evolution during uniaxial deformation of textured Zircaloy-2", *Acta Materialia,* Vol. *56*, No. 14, pp. 3672-3687, 2008.

10. Wu, L., S. R. Agnew, D. W. Brown, G. M. Stoica, B. Clausen, A. Jain, D. E. Fielden and P. K. Liaw, "Internal stress relaxation and load redistribution during the twinning-detwinning-dominated cyclic deformation of a wrought magnesium alloy, ZK60A", *Acta Materialia,* Vol. *56*, No. 14, pp. 3699-3707, 2008.

11. Aydiner, C. C., J. V. Bernier, B. Clausen, U. Lienert, C. N. Tome and D. W. Brown, "Evolution of stress in individual grains and twins in a magnesium alloy aggregate", *Physical Review B,* Vol. *80*, No. 2, pp. 1-6, 2009.

12. Efstathiou, C., H. Sehitoglu and J. Lambros, "Multiscale strain measurements of plastically deforming polycrystalline titanium: Role of deformation heterogeneities", *International Journal of Plasticity,* Vol. *26*, No. 1, pp. 93-106, 2010.

13. Heripre, E., M. Dexet, J. Crepin, L. Gelebart, A. Roos, M. Bornert and D. Caldemaison, "Coupling between experimental measurements and polycrystal finite element calculations for micromechanical study of metallic materials", *International Journal of Plasticity,* Vol. *23*, No. 9, pp. 1512-1539, 2007.

14. Sachtleber, M., Z. Zhao and D. Raabe, "Experimental investigation of plastic grain interaction", *Materials Science and Engineering a-Structural Materials Properties Microstructure and Processing,* Vol. *336*, No. 1-2, pp. 81-87, 2002.

15. Bodelot, L., E. Charkaluk, L. Sabatier and P. Dufrenoy, "Experimental study of heterogeneities in strain and temperature fields at the microstructural level of polycrystalline metals through fully-coupled full-field measurements by Digital Image Correlation and Infrared Thermography", *Mechanics of Materials,* Vol. *43*, No. 11, pp. 654-670, 2011.

16. Delaire, F., J. L. Raphanel and C. Rey, "Plastic heterogeneities of a copper multicrystal deformed in uniaxial tension: Experimental study and finite element simulations", *Acta Materialia,* Vol. *48*, No. 5,pp. 1075-1087, 2000.

17. Tatschl, A. and O. Kolednik, "On the experimental characterization of crystal plasticity in polycrystals", *Materials Science and Engineering: A,* Vol. *356*, No. 1-2, pp. 447-463, 2003.

18. Schroeter, B. M. and D. L. McDowell, "Measurement of deformation fields in polycrystalline OFHC copper", *International Journal of Plasticity,* Vol. *19*, No. 9, pp. 1355-1376, 2003.

19. Padilla, H. A., J. Lambros, A. J. Beaudoin and I. M. Robertson, "Relating inhomogeneous deformation to local texture in zirconium through grain-scale digital image correlation strain mapping experiments", *International Journal of Solids and Structures,* Vol. *49*, No. 1, pp. 18-31, 2012.

20. Efstathiou, C. and H. Sehitoglu, "Strain hardening and heterogeneous deformation during twinning in Hadfield steel", *Acta Materialia,* Vol. *58*, No. 5, pp. 1479-1488, 2010.

21. Brandon D, K. W. D., *Microstructural Characterization of Materials*, John Wiley & Sons, England, 2008.

22. Christian, J. W. and S. Mahajan, "Deformation Twinning", *Progress in Materials Science,* Vol. *39*, No. 1-2, pp. 1-157, 1995.

23. Yoo, M. H. and J. K. Lee, "Deformation twinning in HCP metals and alloys", *Philosophical Magazine A (Physics of Condensed Matter, Defects and Mechanical Properties),* Vol. *63*, No. 5, pp. 987-1000, 1991.

24. Kim D.H., M. M. V., Ebrahimi F., Tulenko J.S., Phillpot S.R., "Deformation processes in [1120]-textured nanocrystalline Mg by molecular dynamics simulation", *Acta Materialia,* Vol. *58*, No. 19, pp. 6217–6229, 2010.

25. Beyerlein, I. J., R. J. McCabe and C. N. Tome, "Effect of microstructure on the nucleation of deformation twins in polycrystalline high-purity magnesium: A multi-scale

modeling study", *Journal of the Mechanics and Physics of Solids,* Vol. *59*, No. 5, pp. 988-1003, 2011.

26. Chu, T. C., W. F. Ranson, M. A. Sutton and W. H. Peters, "Applications of digital-image-correlation techniques to experimental mechanics", *Experimental Mechanics,* Vol. *25*, No. 3, pp. 232-44, 1985.

27. Vendroux, *Correlation: A Digital Image Correlation Program For Displacement and Displacement Gradient Measurement*, California, 1990.

28. Sutton, M. A., J.-J. Orteu and H. W. Shreier, *Image Correlation for Shape, Motion and Deformation Measurements: Basic Concepts,Theory and Applications*, Springer, New York, NY, 2010.

29. Inc, C. S., *Principle of Digital Image Correlation,* 2010, http://www.correlatedsolutions.com/index.php/principle-of-digital-image-correlation, accesed at September 2011.

30. Willems, A., S. V. Lomov, I. Verpoest and D. Vandepitte, "Drape-ability characterization of textile composite reinforcements using digital image correlation", *Optics and Lasers in Engineering,* Vol. *47*, No. 2-3, pp. 343-351, 2009.

31. Jin, H., W. Y. Lu and J. Korellis, "Micro-scale deformation measurement using the digital image correlation technique and scanning electron microscope imaging", *Journal of Strain Analysis for Engineering Design,* Vol. *43*, No. 8, pp. 719-728, 2008.

32. Scrivens, W. A., Y. Luo, M. A. Sutton, S. A. Collette, M. L. Myrick, P. Miney, P. E. Colavita, A. P. Reynolds and X. Li, "Development of patterns for digital image correlation measurements at reduced length scales", *Experimental Mechanics,* Vol. *47*, No. 1, pp. 63-77, 2007.

33. Jonnalagadda, K. N., I. Chasiotis, S. Yagnamurthy, J. Lambros, J. Pulskamp, R. Polcawich and M. Dubey, "Experimental Investigation of Strain Rate Dependence of Nanocrystalline Pt Films", *Experimental Mechanics,* Vol. *50*, No. 1, pp. 25-35, 2010.

34. Zhang, D. S., M. Luo and D. D. Arola, "Displacement/strain measurements using an optical microscope and digital image correlation", *Optical Engineering,* Vol. *45*, No. 3, pp. 1-9, 2006.

35. Dautriat, J., M. Bornert, N. Gland, A. Dimanov and J. Raphanel, "Localized deformation induced by heterogeneities in porous carbonate analysed by multi-scale digital image correlation", *Tectonophysics,* Vol. *503*, No. 1-2, pp. 100-116, 2011.

36. Collette, S. A., M. A. Sutton, P. Miney, A. P. Reynolds, X. D. Li, P. E. Colavita, W. A. Scrivens, Y. Luo, T. Sudarshan, P. Muzykov and M. L. Myrick, "Development of patterns for nanoscale strain measurements: I. Fabrication of imprinted Au webs for polymeric materials", *Nanotechnology,* Vol. *15*, No. 12, pp. 1812-1817, 2004.

37. Tanaka, Y., K. Naito, S. Kishimoto and Y. Kagawa, "Development of a pattern to measure multiscale deformation and strain distribution via in situ FE-SEM observations", *Nanotechnology,* Vol. *22*, No. 11, pp., 2011.

38. Xu, Z. H., X. D. Li, M. A. Sutton and N. Li, "Drift and spatial distortion elimination in atomic force microscopy images by the digital image correlation technique", *Journal of Strain Analysis for Engineering Design,* Vol. *43*, No. 8, pp. 729-743, 2008.

39. Schreier, H. W., D. Garcia and M. A. Sutton, "Advances in light microscope stereo vision", *Experimental Mechanics,* Vol. *44*, No. 3, pp. 278-288, 2004.

40. Abuzaid, W. Z., M. D. Sangid, J. D. Carroll, H. Sehitoglu and J. Lambros, "Slip transfer and plastic strain accumulation across grain boundaries in Hastelloy X", *Journal of the Mechanics and Physics of Solids,* Vol. *60*, No. 6, pp. 1201-1220, 2012.

41. Carroll, J., C. Efstathiou, J. Lambros, H. Sehitoglu, B. Hauber, S. Spottswood and R. Chona, "Investigation of fatigue crack closure using multiscale image correlation experiments", *Engineering Fracture Mechanics,* Vol. *76*, No. 15, pp. 2384-2398, 2009.

42. Hamilton, R. F., H. Sehitoglu, K. Aslantas, C. Efstathiou and H. J. Maier, "Inter-martensite strain evolution in NiMnGa single crystals", *Acta Materialia,* Vol. *56*, No. 10, pp. 2231-2236, 2008.

43. Carroll, J., W. Abuzaid, J. Lambros and H. Sehitoglu, "An experimental methodology to relate local strain to microstructural texture", *Review of Scientific Instruments,* Vol. *81*, No. 8, pp. 9, 2010.

44. Tong, W., "Detection of plastic deformation patterns in a binary aluminum alloy", *Experimental Mechanics,* Vol. *37*, No. 4, pp. 452-459, 1997.

45. Li, E. B., A. K. Tieu and W. Y. D. Yuen, "Application of digital image correlation technique to dynamic measurement of the velocity field in the deformation zone in cold rolling", *Optics and Lasers in Engineering,* Vol. *39*, No. 4, pp. 479-488, 2003.

46. Kocks, U. F., C. N. Tome and H.-R. Wenk, *Texture and Anisotropy: Preferred orientations in polycrystals and their effect and materials properties*, Cambridge University Press, Cambridge, 1998.

47. Brandon David, K. W. D., *Microstructural Characterization of Materials*, 2nd ed., John Wiley & Sons, England, 2010.

48. Randle Valerie, E. O., *Introduction to Texture Analysis,* CRC Press, Florida, 2000.

49. Vendroux, G. and W. G. Knauss, "Submicron deformation field measurements: Part 2. Improved digital image correlation", *Experimental Mechanics,* Vol. *38*, No. 2, pp. 86-92, 1998.

50. MguilTouchal, S., F. Morestin and M. Brunet, *Various experimental applications of digital image correlation method*, Computational Mechanics Publications Ltd, Southampton, 1997.